

CoViS-Net: A Cooperative Visual Spatial Foundation Model for Multi-Robot Applications

Jan Blumenkamp, Steven Morad, Jennifer Gielis, Amanda Prorok
University of Cambridge, Department of Computer Science and Technology
{jb2270, sm2558, jag233, asp45}@cam.ac.uk

Abstract—Spatial understanding from vision is crucial for robots operating in unstructured environments. In the real world, spatial understanding is often an ill-posed problem. There are a number of powerful classical methods that accurately regress relative pose, however, these approaches often lack the ability to leverage data-derived priors to resolve ambiguities. In multi-robot systems, these challenges are exacerbated by the need for accurate and frequent position estimates of cooperating agents. To this end, we propose CoViS-Net, a cooperative, multi-robot, visual spatial foundation model that learns spatial priors from data. Unlike prior work evaluated primarily on offline datasets, we design our model specifically for online evaluation and real-world deployment on cooperative robots. Our model is completely decentralized, platform agnostic, executable in real-time using onboard compute, and does not require existing network infrastructure. In this work, we focus on relative pose estimation and local Bird’s Eye View (BEV) prediction tasks. Unlike classical approaches, we show that our model can accurately predict relative poses without requiring camera overlap, and predict BEVs of regions not visible to the ego-agent. We demonstrate our model on a multi-robot formation control task outside the confines of the laboratory.

I. INTRODUCTION

Spatial understanding is a cornerstone of robotic operation in unstructured environments, relying on effective pose estimation and environmental perception [48, 46, 8, 58, 49, 7, 28, 29]. While traditional methods leveraging GNSS, LiDAR, Time of Flight (ToF), and Ultra-Wide Band (UWB) sensors have been instrumental in advancing robotics, they often come with constraints (e.g., indoor, outdoor, sunny, IR-reflective surfaces, etc.). Unlike these methods, color cameras offer a low-cost, energy-efficient, and rich data source suitable for many environments, aligned with the vision-centric design principles of real-world, human-designed environments.

Classical vision-based techniques such as Visual Odometry [48], Visual SLAM [7], and Structure-from-Motion [49], struggle with the inherent ill-posed nature of spatial tasks, lacking the capability to integrate human-like semantic priors to resolve ambiguous situations. These challenges are exacerbated in multi-robot applications, requiring not only environmental spatial understanding but also rapid and accurate relative pose estimates to other robots, as seen in scenarios such as flocking [39], path planning [50], and collaborative perception [69]. Explicit detection of other agents is a viable alternative [58, 8, 46, 28, 29], but requires line-of-sight measurements and is not platform agnostic. On the other hand, deep pose predictors demonstrate the ability to

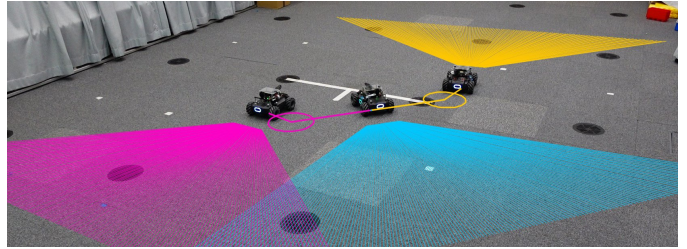


Fig. 1. Our model can be used to control the relative pose (yellow and purple circle) of multiple follower robots (yellow and purple cone) to a leader robot (with blue cone) following a reference trajectory using visual cues in the environment only. Even if there is no direct visual overlap (cone intersection), the model is able to correctly estimate the relative pose.

learn human priors to solve complex spatial tasks [27, 37, 63, 64, 6, 3, 40]. Unfortunately, such methods have yet to be broadly integrated and demonstrated on robots in real-world scenarios – particularly when operating under hardware or computational constraints. When considering *multi-robot* systems, prior assumptions on data availability and latency are broken, and otherwise promising work fails to deliver. Furthermore, *uncertainty metrics* are essential to reason about the reliability of predictions.

Acknowledging these limitations, our work introduces CoViS-Net, a decentralized, platform-agnostic visual spatial foundation model designed for real-world multi-robot applications. *This model operates in real-time on onboard computers without the need for pre-existing static network infrastructure, thus addressing critical scalability, deployment flexibility, and operational robustness challenges.*

We design a deep distributed stateless architecture to focus on the challenges specific to multi-robot systems, including the need for relative pose estimation [39, 50, 56, 26, 67] and the prediction of BEVs of regions without local camera coverage [21, 43, 62, 22]. We demonstrate the efficacy of our approach through real-world applications, showcasing its use on a multi-robot control task outside laboratory settings.

In summary, our contributions are threefold:

- 1) A novel architecture for platform-agnostic, decentralized, real-time, multi-robot pose estimation from monocular images, incorporating uncertainty awareness without the need for a predefined map.
- 2) Extension of this architecture to predict uncertainty-aware BEVs, enhancing spatial understanding in multi-robot systems, especially in occluded or unobserved

areas.

- 3) Real-world validation of our model’s applicability to multi-robot control and BEV estimation, even for ill-posed situations *where images share no overlap*.

II. RELATED WORK

Multi-Robot Systems: Multi-robot systems necessitate the coordination of multiple, often fast-moving robots within close proximity in real-world settings. This coordination requires not only a spatial understanding of the immediate environment but also accurate and quick pose estimates of cooperating robots. Key applications include flocking, where agents maintain proximity using rules of separation, alignment, and cohesion [39]; formation control, where agents maintain or adjust formations to navigate obstacles [31]; and trajectory de-confliction to prevent agent collisions (RVO) [56]. Additional scenarios involve multi-agent object manipulation [26, 2] and area coverage [67, 51]. Recent advances employ Graph Neural Networks (GNNs) for enhanced multi-agent control and cooperative perception, facilitating inter-robot communication through latent messages to address partial knowledge challenges [55, 14, 15, 5, 4, 59, 69, 21, 43, 62, 22]. A significant gap in this research area is the acquisition and reliance on pose knowledge, typically relative pose, which we address in this paper. For learning-based approaches, our model can be used as a plug-in model to fine-tune for more specific use cases.

Map-Free Relative Pose Regression: Map-Based Pose Regression, as in [18, 45], predicts a camera image’s pose within a learned model of a scene. Conversely, Map-Free Relative Pose Regression, exemplified by [3], estimates the relative pose between two camera images without needing scene-specific training. Feature matching between images retrieves orientation and a scale-less transformation vector. Traditional non-learning methods like SIFT [25] handle images with significant overlap and minimal differences effectively. However, learning-based approaches for feature matching, such as Superglue [44], LOFTR [53], Gluestick [33], and Lightglue [23], have gained popularity, even though they still require considerable visual overlap. Integrating scale is possible by pairing these methods with depth maps or directly through Siamese network architectures that use dual CNNs for image encoding and pose estimation via a fully connected layer [27, 20, 12, 1, 63, 37, 64]. These models, generally assuming visual overlap and using mean-squared-error loss, lack uncertainty estimates, limiting their applicability to robotics. Robotics applications of similar methods [63, 37, 64] have not been tested in real deployments. To the best of our knowledge, Winkelbauer et al. [61] is the only method to employ uncertainty estimation in robot localization through Monte Carlo dropout, which is an epistemic uncertainty. In this work, we introduce a method to predict aleatoric uncertainties. Extending beyond field-of-view pose prediction, [6] and [3] proposed novel rotation and position estimation methods in challenging scenarios. Learning-based limitations are highlighted by [68], advocating for essential matrix estimation, and [40], using vision transformers for direct essential matrix es-

imation. Our approach diverges from this prior body of work by providing reliable relative poses with uncertainty estimates, without requiring visual overlap, and using unmodified pre-trained foundation models, enabling transfer learning [60].

BEV Prediction: In autonomous vehicle applications, detailed environmental representation is crucial. The BEV, merging data from diverse sensors in an agent-centric frame, is particularly effective. Traditional BEV generation involves multiple steps, but deep-learning approaches have shown promise. Pioneers like Roddick and Cipolla [41] projected image features into a BEV representation for prediction. The Lift, Splat, Shoot methodology by Phillion and Fidler [36] adopted a novel multi-camera rig approach. BEVFormer [65], PETR [24], and BEVSegformer [34] contributed new dimensions, such as spatiotemporal information and multi-task learning. Extensions to multi-agent scenarios [62, 43, 21, 22, 59, 16] predominantly relied on GNSS for global pose knowledge. Inspired by Dutta et al. [11], our work employs a transformer-based BEV predictor, mapping transformer output sequences directly to a BEV grid. We focus on a 6m x 6m indoor area, unlike the larger scales typical in autonomous driving. Beyond [11], we integrate pose embeddings from our estimator into multi-node feature aggregation, showing how the infusion of explicit pose information provides benefits over simple aggregation.

III. PROBLEM FORMULATION

Given a multi-robot system, our goal is (i) for each robot to predict its pose with respect to other robots based only on non-line-of-sight visual correspondences in the environment, and (ii) to use this information for downstream tasks, such as for estimating a local occupancy grid map or for real-time multi-robot control in transfer learning [60].

Consider a multi-robot system represented by a set of nodes \mathcal{V} . Each node $v_i \in \mathcal{V}$ has a position $\mathbf{p}_{w,i}$ and an orientation $\mathbf{R}_{w,i}$ in the world coordinate frame \mathcal{F}_w . The set of edges $\mathcal{E} \subseteq \mathcal{V} \times \mathcal{V}$, defined by the communication topology, connects nodes v_i to v_j and defines the graph $\mathcal{G} = (\mathcal{V}, \mathcal{E})$. For each edge $(v_i, v_j) \in \mathcal{E}$, the relative position of v_j in the coordinate frame of v_i (denoted as \mathcal{F}_i) is $\mathbf{p}_{i,ij} = \mathbf{R}_{w,i}^{-1} \cdot (\mathbf{p}_{w,j} - \mathbf{p}_{w,i})$, and the relative rotation is $\mathbf{R}_{i,ij} = \mathbf{R}_{w,i}^{-1} \cdot \mathbf{R}_{w,j}$.

Each node v_i is equipped with a camera C_i , located and oriented identically to the robot. The camera output at node v_i is represented as an image I_i . From the images, we must estimate relative poses and associated uncertainties $(\hat{\mathbf{p}}_{i,ij}, \hat{\mathbf{R}}_{i,ij}, \sigma_{ij}^2) \forall v_j \in \mathcal{N}(v_i)$ with respect to v_i in its coordinate frame \mathcal{F}_i . Notably, we do not assume that there is overlap between images, nor line-of-sight positioning between robots. Relying exclusively on common image features makes this approach platform-agnostic and only requires a single monocular camera. Utilizing these estimated poses, the robots are tasked to cooperatively generate a BEV $\hat{\mathbf{B}}\hat{\mathbf{E}}\hat{\mathbf{V}}_i$ around each v_i . The pose estimates and BEV can be used as input for a wide range of downstream multi-robot applications.

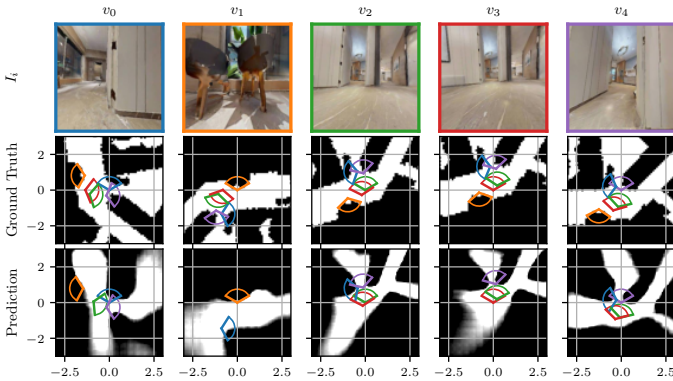


Fig. 2. We visualize a sample from the simulation validation dataset $\mathcal{D}_{\text{Val}}^{\text{Sim}}$ for five nodes, corresponding to the five columns. Each node is associated with the colored border in the first row. The top row shows the camera image I_i from the perspective of each node. The middle row shows the ground truth labels for each respective node in the coordinate system \mathcal{F}_i . Each robot is centered in its coordinate frame, facing upwards at position $(0, 0)$. The ground truth poses $\mathbf{p}_{i,j}$ of the other robots are indicated, together with their field of view. The background shows the BEV map BEV_i for each robot. The bottom row shows the corresponding predictions for each robot. We only show pose predictions $\hat{\mathbf{p}}_{i,j}, \hat{\mathbf{R}}_{i,j}$ with a sufficiently low uncertainty σ_{ij}^2 . In the background, the predicted corresponding BEV $\hat{\text{BEV}}_i$ is shown.

IV. MODEL TRAINING

In this section, we explain the whole training pipeline of our foundation model. We generate a simulation dataset and define our model architecture before we introduce our uncertainty estimation strategy and training protocol.

A. Dataset

We utilize the Habitat simulator [47, 54] along with the training set of the HM3D dataset [38], which comprises 800 scenes of 3D-scanned real-world multi-floor buildings. We select Habitat and HM3D for their photorealism and the availability of ground-truth pose information, as well as detailed navigation mesh information that can be converted to a BEV of the scene. We instantiate a single agent equipped with a calibrated camera with a field of view of 120° . For each scene, we randomly sample several uniform agent positions based on the total area of the scene. For each sample, the camera orientation is randomized across all three axes. Additionally, for each scene, we extract the processed navigation mesh, which indicates areas that are navigable by a mobile robot, or not navigable due to obstacles or overhangs. In total, we extract 3,816,288 images from 1,411 floors in 800 scenes.

We divide this data into training $\mathcal{D}_{\text{Train}}^{\text{Sim}}$ (80%), testing $\mathcal{D}_{\text{Test}}^{\text{Sim}}$ (19%), and validation $\mathcal{D}_{\text{Val}}^{\text{Sim}}$ (1%) sets. From these sets, we sample pairs of $N_{\text{max}} = 5$ images and poses by (1) uniformly sampling 25% of individual images from each dataset, and then (2) uniformly sampling $N_{\text{max}} - 1$ images within a distance of $d_{\text{max}} = 2$ m around each sample from (1). This process yields 763,257 training and 276,680 test tuples, each of which are at most $2d_{\text{max}}$ apart and pointing in random directions, thus providing realistically close and distant data samples for estimating both poses and uncertainties in case of no overlaps.

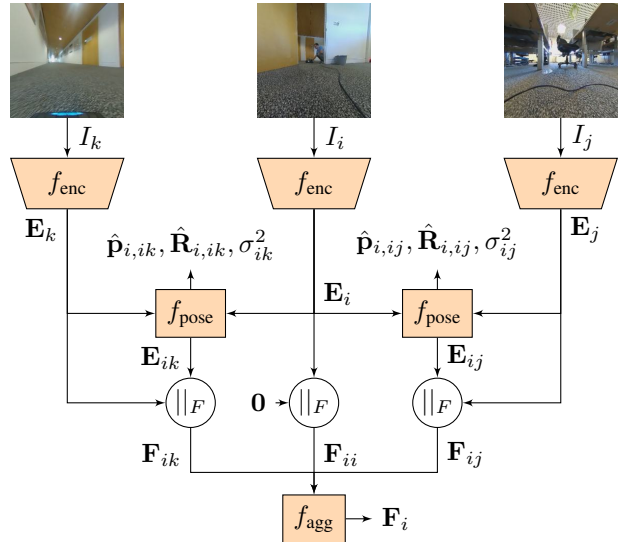


Fig. 3. Overview of the model architecture: We illustrate the decentralized evaluation with respect to v_i , which receives embeddings $\mathbf{E}_i, \mathbf{E}_j$ generated by the encoder f_{enc} from the neighbors $v_j, v_k \in \mathcal{N}(v_i)$. For each received embedding, we employ f_{pose} to compute the pose. This pose can then be utilized for pose control or any other relevant task. We concatenate the pose embedding \mathbf{E}_{ij} with the image embedding \mathbf{E}_i and subsequently aggregate this into a node feature \mathbf{F}_i .

The ground truth BEV BEV_i is a cropped $6 \text{ m} \times 6 \text{ m}$ view of the floor’s BEV around v_i , generated through Habitat’s navigation mesh. Each agent v_i is centered and facing north.

B. Model

We employ three models: f_{enc} , f_{pose} , and f_{agg} . The encoder f_{enc} generates a common embedding of images, f_{pose} performs a pairwise estimate of poses, and f_{agg} spatially aggregates node features based on the output from f_{pose} . An overview of the model architecture is provided in Fig. 3.

Transformers: Our methodology utilizes the Transformer architecture [57], distinguished by its self-attention mechanism. This mechanism computes the output as a weighted sum of the values (\mathbf{V}), with the weights determined by the compatibility of queries (\mathbf{Q}) and keys (\mathbf{K}) as per the formula: $\text{Attention}(\mathbf{Q}, \mathbf{K}, \mathbf{V}) = \text{softmax}((\mathbf{Q}\mathbf{K}^T)/\sqrt{d_k})\mathbf{V}$, where d_k is the dimensionality of the keys. Typically, \mathbf{Q} , \mathbf{K} , and \mathbf{V} are set to the same input features. Therefore, we refer to one attention block as f_{attn} and to an instance of a multi-layer transformer, including both the attention mechanism and a position-wise feed-forward network, as $f_{\text{trans}}^{\text{inst}}$.

The Vision Transformer (ViT) [10] extends this architecture to images by dividing an image into patches treated as a sequence.

Image encoder: We use DinoV2 [32] as a pre-trained encoder. DinoV2 is a vision foundation model based on ViT and pre-trained in a self-supervised manner on the LVD-142M dataset, which is a cumulation of various filtered datasets, including various versions of ImageNet [9] and Google Landmarks. We specifically chose DinoV2 due to its pre-training on a wide variety of images and demonstrated powerful feature

representation as well as demonstrated depth understanding of scenes. We use the smallest distilled version of DinoV2 based on ViT-S/14 with 22.1 M parameters for performance reasons. We refer to this model as f_{dino} .

For explicit communication, agents utilize a one-hop communication network, detailed further in Sec. V-C. Each node v_i processes the image I_i through the encoder function f_{enc} to generate a node embedding $\mathbf{E}_i \in \mathbb{R}^{S \times F}$, which constitutes the sole information communicated to and utilized by neighboring nodes. Here, S represents the sequence length (which can be reduced to adjust model performance, as explained in Sec. V), and F denotes the size of each feature vector in the sequence.

The weights in f_{dino} are frozen, and an instance of $f_{\text{trans}}^{\text{enc}}$, which is trained, is concatenated, resulting in f_{enc} (Eq. 2).

$$f_{\text{enc}} = f_{\text{dino}} \cdot f_{\text{trans}}^{\text{enc}} \quad (1)$$

$$f_{\text{enc}}(I_i) = \mathbf{E}_i \quad (2)$$

Freezing the weights of f_{dino} facilitates the ability to use the raw output used independently of our proposed foundation model, meaning that a wide variety of open-source fine-tuned image detectors can be leveraged without running an additional forward pass.

Pairwise pose encoder: Our goal is to develop a pose prediction function, f_{pose} . At each root node v_i , we generate an image encoding \mathbf{E}_i using f_{enc} . This encoding \mathbf{E}_i is transmitted to neighboring nodes. Given the root and neighbor encodings \mathbf{E}_i and \mathbf{E}_j , f_{pose} estimates the pose of each neighbor relative to the root node. Specifically, for a given root node v_i and each neighbor v_j , f_{pose} calculates the set of estimated relative poses and uncertainties $(\hat{\mathbf{p}}_{i,ij}, \hat{\mathbf{R}}_{i,ij}, \sigma_{ij}^2) : \forall v_j \in \mathcal{N}(v_i)$, with respect to v_i in the coordinate frame \mathcal{F}_i , as well as edge embeddings $\mathbf{E}_{ij} : \forall v_j \in \mathcal{N}(v_i)$.¹

We define the concatenation operation of two tensors \mathbf{A} and \mathbf{B} along axis C as $(\mathbf{A} \parallel_C \mathbf{B})$ and the indexing operation on tensor \mathbf{A} by the first element along axis B as \mathbf{A}_{B1} . We introduce an instance of another transformer $f_{\text{trans}}^{\text{pose}}$, and four MLPs $f_p^\mu, f_p^\sigma, f_R^\mu, f_R^\sigma$. Furthermore, we introduce a learnable transformer positional embedding for the sequence dimension \mathbf{S}_{pose} . For each incoming $\mathbf{E}_j \forall v_j \in \mathcal{N}(v_i)$, we perform a pose estimation as

$$\mathbf{E}_{ij} = f_{\text{trans}}^{\text{pose}}((\mathbf{E}_i \parallel_S \mathbf{E}_j) + \mathbf{S}_{\text{pose}})_{S1} \quad (3)$$

$$\hat{\mathbf{p}}_{i,ij}, \hat{\mathbf{R}}_{i,ij} = f_p^\mu(\mathbf{E}_{ij}), f_R^\mu(\mathbf{E}_{ij}) \quad (4)$$

$$\sigma_{p,ij}^2, \sigma_{R,ij}^2 = f_p^\sigma(\mathbf{E}_{ij}), f_R^\sigma(\mathbf{E}_{ij}) \quad (5)$$

$$\sigma_{ij}^2 = (\sigma_{p,ij}^2, \sigma_{R,ij}^2) \quad (6)$$

$$f_{\text{pose}}(\mathbf{E}_i, \mathbf{E}_j) = (\hat{\mathbf{p}}_{i,ij}, \hat{\mathbf{R}}_{i,ij}, \sigma_{ij}^2).$$

We concatenate the node features along the sequence dimension, add the positional embedding, run the transformer

and then extract the first element of the sequence dimension (Eq. 3), and eventually use this edge embedding to estimate poses and orientations (Eq. 4) and uncertainties (Eq. 5 and Eq. 6).

Multi-node aggregation: Lastly, we perform the position-aware feature aggregation, utilizing the node embeddings \mathbf{E}_j generated in f_{pose} for each corresponding edge. The feature aggregation function f_{agg} integrates information from the set of nodes $v_j \in \mathcal{N}(v_i) \cup \{v_i\}$. The resulting output is a feature vector \mathbf{F}_i for each node v_i , encapsulating the aggregated information from its local vicinity, which can be used for any downstream task in a transfer-learning context [60], requiring geometric information in a robotic swarm, for example, to predict a BEV of the environment around the robot that captures areas that might not necessarily be visible by the robot itself.

We introduce an instance of two more transformers $f_{\text{trans}}^{\text{agg}}$ and $f_{\text{trans}}^{\text{post}}$, an MLP f_{aggpos} , a learnable transformer positional embedding \mathbf{S}_{agg} , as well as a BEV decoder f_{BEV} . We perform the node aggregation as

$$\mathbf{X}_{ij} = ((\mathbf{E}_i \parallel_S \mathbf{E}_j) + \mathbf{S}_{\text{agg}}) \quad (7)$$

$$\mathbf{F}_{ij} = (\mathbf{X}_{ij} \parallel_F f_{\text{aggpos}}(\mathbf{E}_{ij})) \quad (8)$$

$$\mathbf{F}_{ii} = (\mathbf{X}_{ii} \parallel_F f_{\text{aggpos}}(\mathbf{0})) \quad (9)$$

$$\mathbf{F}_i = f_{\text{trans}}^{\text{post}} \left(\sum_{v_j \in \mathcal{N}(v_i) \cup \{v_i\}} f_{\text{trans}}^{\text{agg}}(\mathbf{F}_{ij}) \right)_{S1} \quad (10)$$

$$\hat{\text{BEV}}_i = f_{\text{BEV}}(\mathbf{F}_i). \quad (11)$$

We concatenate the node features along the sequence dimension and add the positional embedding (Eq. 7). We then concatenate a nonlinear transformation of the edge features along the feature dimension to the output of the previous operation (Eq. 8). The previous operations are performed for all $v_j \in \mathcal{N}(v_i)$, but it is essential to include self-loops to the graph topology, as a full forward pass of the neural network would otherwise not be possible if $\mathcal{N}(v_i)$ were empty. We therefore set the edge embedding to the zero tensor $\mathbf{0}$ in that case (Eq. 8). We then aggregate over the set of neighbors and itself to produce the output embedding (Eq. 10) and finally use this to estimate any other downstream task, for example, estimating a BEV (Eq. 11).

C. Training

For training our models, we resort to supervised learning. This section describes the losses as well as our approach to estimating uncertainty.

Uncertainty estimation: In general, two kinds of uncertainties can be modeled. While *epistemic uncertainty* captures uncertainty in the model, i.e. uncertainty that can be improved by training the model on more data, *aleatoric uncertainty* captures noise inherent to a specific observation [17]. We argue that for estimating poses and applications to pose control in a robotic system, aleatoric uncertainty is much more important than epistemic uncertainty since a downstream

¹Although image overlap is not a strict assumption, our uncertainty measure σ_{ij}^2 enables us to identify image pairs that are unsuitable for joint estimation due to lack of feature correspondence, thus allowing the application to react accordingly, e.g., prioritize rotational alignment over positional alignment to regain certainty.

application can *act* on the predicted aleatoric uncertainty to *decrease* it. Approaches such as Monte Carlo Dropout [13] or Model Ensembles [19] have previously used in similar applications [61], but these approaches model the epistemic uncertainty. Instead, we propose to use the Gaussian Negative Log Likelihood Loss, as introduced by Nix and Weigend [30] and revisited by Kendall and Gal [17]. As a generalization of the mean squared error (MSE) loss, it allows the model to not only predict a mean $\hat{\mu}$, but also a variance $\hat{\sigma}^2$, which is learned from data points μ . The loss is defined as

$$\mathcal{L}_{\text{GNLL}}(\mu, \hat{\mu}, \hat{\sigma}^2) = \frac{1}{2} \left(\log(\hat{\sigma}^2) + \frac{(\hat{\mu} - \mu)^2}{\hat{\sigma}^2} \right), \quad (12)$$

where intuitively, the left component penalizes predictions of high variance, while the right component scales the MSE loss by the predicted variance to penalize errors more when the predicted uncertainty is low.

Estimating Rotations: Estimating rotation is inherently difficult due to discontinuities that occur in many orientation representations. In machine learning, quaternions are typically chosen to represent rotations due to their numerical efficiency and lack of singularities. Peretroukhin et al. [35] propose to represent rotations through a symmetric matrix that defines a Bingham distribution over unit quaternions, which allows them to predict epistemic uncertainty. To obtain an aleatoric uncertainty for the rotation, we combine Eq. 14 with Eq. 12 and let the model predict one variance for the rotation estimate, as shown in Eq. 15.

$$d_{\text{quat}}(\hat{\mathbf{q}}, \mathbf{q}) = \min(\|\mathbf{q} - \hat{\mathbf{q}}\|_2, \|\mathbf{q} + \hat{\mathbf{q}}\|_2) \quad (13)$$

$$\mathcal{L}_{\text{chord}}^2(\hat{\mathbf{q}}, \mathbf{q}) = 2d_{\text{quat}}^2(\hat{\mathbf{q}}, \mathbf{q}) (4 - d_{\text{quat}}^2(\hat{\mathbf{q}}, \mathbf{q})) \quad (14)$$

$$\mathcal{L}_{\text{chord}}^{\text{GNLL}}(\mathbf{q}, \hat{\mathbf{q}}, \hat{\sigma}^2) = \frac{1}{2} \left(\log(\hat{\sigma}^2) + \frac{\mathcal{L}_{\text{chord}}^2(\hat{\mathbf{q}}, \mathbf{q})}{\hat{\sigma}^2} \right) \quad (15)$$

BEV prediction: For the BEV prediction, we use a combination of the Dice loss [52] $\mathcal{L}_{\text{Dice}}$ and Binary Cross Entropy (BCE) Loss \mathcal{L}_{BCE} to achieve sharp and clear predictions. The BEV loss is defined as

$$\begin{aligned} \mathcal{L}_{i,\text{BEV}} = & \alpha \cdot \mathcal{L}_{\text{Dice}}(\text{BEV}_i, \hat{\text{BEV}}_i) \\ & + (1 - \alpha) \cdot \mathcal{L}_{\text{BCE}}(\text{BEV}_i, \hat{\text{BEV}}_i), \end{aligned} \quad (16)$$

where $0 \leq \alpha \leq 1$ balances between the Dice and BCE objectives.

Training: We define the pose loss as

$$\begin{aligned} \mathcal{L}_{i,ij,\text{Pose}} = & \mathcal{L}_{\text{GNLL}}(\mathbf{p}_{i,ij}, \hat{\mathbf{p}}_{i,ij}, \sigma_{\mathbf{p},ij}^2) \\ & + \beta \mathcal{L}_{\text{chord}}^{\text{GNLL}}(\mathbf{R}_{i,ij}, \hat{\mathbf{R}}_{i,ij}, \sigma_{\mathbf{R},ij}^2), \end{aligned} \quad (17)$$

where $0 \leq \beta \leq 1$ balances between the position and orientation loss, and, lastly, the total loss over the graph as

$$\mathcal{L} = \sum_{v_i \in \mathcal{V}} \left(\mathcal{L}_{i,\text{BEV}} + \sum_{v_j \in \mathcal{N}(v_i)} \mathcal{L}_{i,ij,\text{Pose}} \right). \quad (18)$$

We find that the uncertainty terms in the loss are necessary for training, as many samples within the dataset do not contain overlaps, and are sometimes in two different (yet adjacent) rooms. Otherwise, the error from these difficult samples would dwarf the error from other samples, hampering learning.

We use Pytorch Lightning to train our model for 15 epochs on two NVidia A100 GPUs. This training takes approximately 24 hours. We optimize the weights using the AdamW optimizer and use the 1cycle learning rate annealing schedule throughout the training and configured weight decay. We choose the best model based on the performance on the validation set. We provide further details about the training procedure in the supplementary materials.

After training the model on $\mathcal{D}_{\text{Train}}^{\text{Sim}}$, we freeze the weights and perform no further sim-to-real finetuning, thus zero-shot transferring from simulation to real-world evaluation.

V. EXPERIMENTS AND RESULTS

We demonstrate the performance of our trained models on a simulated testset $\mathcal{D}_{\text{Test}}^{\text{Sim}}$ and new real-world test sets $\mathcal{D}_{\text{Test}}^{\text{Real}}$, introduced in this section. First, we outline the metrics we use. Then, we discuss our simulation experiments and results. Next, we collect real-world images using our multirobot system, and analyze the model performance. Finally, we compile and deploy our model on a real-time trajectory tracking task, and report our findings.

Metrics: We compute the absolute Euclidean distance between the predicted and ground truth poses and the geodesic distance between rotations as

$$D_{\text{pos}}(\mathbf{p}_{i,ij}, \hat{\mathbf{p}}_{i,ij}) = \|\mathbf{p}_{i,ij} - \hat{\mathbf{p}}_{i,ij}\|$$

$$D_{\text{rot}}(\mathbf{R}_{i,ij}, \hat{\mathbf{R}}_{i,ij}) = 4 \cdot \arcsin \left(\frac{1}{2} d_{\text{quat}}(\hat{\mathbf{R}}_{i,ij}, \mathbf{R}_{i,ij}) \right)$$

for all edges and report median errors.

For simulation results, we also report the Dice as well as the Intersection over Union (IoU) metric.

A. Simulation

We conducted a series of experiments across various models trained with different parameters to showcase our model’s efficiency. The quantitative results are presented in Tab. I and Tab. II, with qualitative findings in Fig. 2.

Tab. I details the performance across seven different experiments on the simulation test set $\mathcal{D}_{\text{Test}}^{\text{Sim}}$, as outlined in section Sec. IV-A. We evaluated the impact of image embedding sizes \mathbf{E}_i on communication efficiency, reporting sizes based on 16-bit floats. The Intersection over Union (IoU) and Dice metrics for the BEV representation of the local environment, alongside median pose estimates for all samples in the dataset, are provided. It’s important to note the limitation in reporting estimation feasibility between nodes due to Habitat’s lack of

TABLE I

ABLATION STUDY OVER THE NUMBER OF PATCHES AND SIZE OF FEATURES FOR EACH PATCH. WE REPORT THE BEV PERFORMANCE AS WELL AS THE MEDIAN ERROR FOR POSES ON THE DATASET $\mathcal{D}_{\text{Test}}^{\text{Sim}}$. THE SIZE OF THE EMBEDDING \mathbf{E}_i IS REPORTED IN BYTES.

S	Model		BEV		Median Pose Err.	
	F	Mem	Dice	IoU		
256	48	24 kB	69.1	57.1	36 cm	8.3°
128	96	24 kB	68.8	56.8	40 cm	8.4°
128	48	12 kB	67.9	56.1	38 cm	7.7°
128	24	6 kB	66.7	54.6	50 cm	9.5°
64	48	6 kB	61.0	43.5	51 cm	9.6°
1	3072	6 kB	47.0	1.4	144 cm	89.9°
1	348	696 B	47.1	1.4	84 cm	11.7°

TABLE II

ABLATION OVER DIFFERENT MODES FOR THE BEV PREDICTION ON THE SIMULATION TESTSET $\mathcal{D}_{\text{Test}}^{\text{Sim}}$.

Experiment	Dice	IoU	Median Pose Err.
None	0.628	0.495	N/A
Predicted	0.683	0.561	31 cm, 5.0°
Ground truth	0.743	0.632	0 cm, 0.0°

specific information (e.g., samples facing the same direction might be in adjacent rooms, unseen by the dataset).

Training one model with $F = 48$ and $S = 128$ across $N = 5$ different seeds revealed a very low average standard deviation of 0.011374, leading us to report results for only $N = 1$ seeds in the table for clarity.

The experiments demonstrate that the sequence length S , acting as the context size for each image, significantly influences BEV prediction and pose estimate performance more than feature size F . We set S to 1 for two experiments: (1) we increase F to match the size of the embeddings for the other experiments, and (2) we decrease F , which effectively reduces the transformer to a CNN-only architecture by removing the attention mechanism. This resulted in a marked decrease in performance for both BEV and pose estimations, underscoring the critical role of attention in our model. The best-performing model with $S = 256$ achieved an BEV IoU of 0.571, a Dice score of 0.691, and median pose accuracy of 36 cm and 8.3°. Conversely, models with $S = 1$ showed significant degradation to near unusable BEV predictions and pose errors on the scale of meters. Models with $F = 24$ and $S = 64$ exhibited slightly inferior performance compared to those with larger F or S .

Lastly, we assess the effectiveness of BEV predictions, focusing on the contribution of pose predictions to enhancing BEV accuracy, in an ablation study detailed in Tab. II. We conduct three experiments: (1) A model trained without incorporating any pose prediction into the BEV aggregator. This model can estimate local information and, to a degree, information aggregated through neighbors. However, it must implicitly learn to predict the relative poses between observations to successfully merge the BEV representations from multiple agents. (2) A model trained as described in this work, integrating pose estimates with BEV predictions and aggregating this information from neighbor nodes. For this

experiment, we use the model configuration with $F = 48$ and $S = 128$. (3) A BEV model trained with ground truth pose information from the simulation training set $\mathcal{D}_{\text{Train}}^{\text{Sim}}$. This model’s performance is considered an upper limit, assuming perfect pose estimation. Evaluation on the simulation test set $\mathcal{D}_{\text{Test}}^{\text{Sim}}$ indicates our model performs between the two baselines. It significantly outperforms the pose-free model with an 8.75% improvement in accuracy, while the model using ground truth poses shows an 18.31% performance increase compared to the baseline without pose information. These results highlight the substantial benefit of incorporating pose predictions into BEV estimation, positioning our approach as a notably effective middle ground between the two extremes.

B. Real-World

In this section, we detail our robot setup, custom real-world test set, and model evaluation on this dataset. We run a series of experiments with quantitative results in Tab. III, Tab. VI, Tab. IV, Tab. V, and Fig. 5 and qualitative findings in Fig. 4, Fig. 7, and Fig. 6.

Robot Platform: Our setup includes four DJI RoboMaster S1 robots, each equipped with an NVidia Jetson Orin NX 16GB and a forward-facing calibrated Raspberry Pi HQ camera. The camera’s raw field of view is approximately 170°, rectified to 120° using the OpenCV Fisheye module, with an image resolution of 224×224 px.

Real-World Testset Collection: Our custom real-world test set $\mathcal{D}_{\text{Test}}^{\text{Real}}$ was collected in eight office-like indoor scenes, tailored to our robot platform’s requirements. Unlike existing datasets like Seven Scenes, which have a constrained FOV of 53.8°, our dataset is designed for our model’s application, reflecting dynamic environmental changes through multiple agents. It represents one of the first multi-agent datasets collected with locally connected devices.

Data collection involved a base station with dual cameras and a 2D Lidar, plus a distinctively shaped marker on each robot. We manually navigated robots around the base station to capture a variety of relative poses, then used a custom tool to label Lidar data for pose extraction. In total, we collect 5692 labeled samples. To balance out the distribution of relative positions in the dataset, we sample image pairs to ensure a uniform distribution of relative positions in the range of 0 m to 2 m. We sample a similar number of pairs from all scenes, resulting in a total of 14008 sets of samples each with three images, resulting in a total of $14008 \cdot 2 \cdot 3 = 84048$ pose edges. 32% of these ground truth edges have no visual overlap. We show a sample of each scene from the dataset in Fig. 4. Our dataset covers a diverse and challenging range of indoor scenes, as well as one outdoor scene. We include more details about the testset in the supplementary material.

Metrics: In Tab. III, Tab. VI, Tab. IV and Tab. V, we categorize the median pose error into the categories *Invisible*, *Visible* and *Invisible Filtered*. *Visible* and *Invisible* edges are determined through the FOV overlap (an edge is considered invisible if the angle $D_{\text{rot}}(\mathbf{R}_{i,ij}, \mathbf{0}) > \text{FOV}$). *Invisible Filtered* samples use the predicted position uncertainty $f_p^{\sigma ij}$ of our

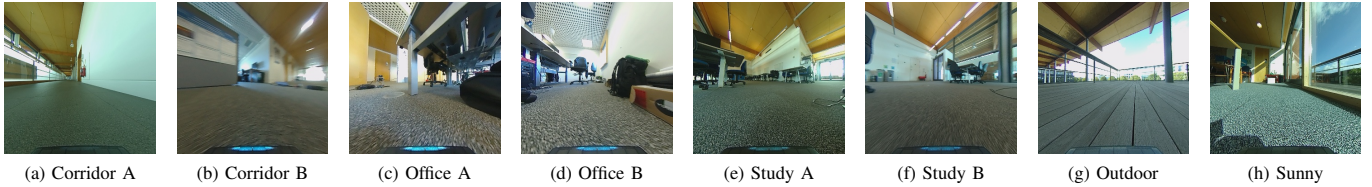


Fig. 4. We collect the real-world dataset $\mathcal{D}_{\text{Test}}^{\text{Real}}$ from five unique scenes in an indoor office building. The scenes show different challenges, from cluttered environments over scenes with high ceilings to sunny floors.

TABLE III

ABLATION STUDY OVER THE NUMBER OF PATCHES AND SIZE OF FEATURES FOR EACH PATCH. WE REPORT THE BEV PERFORMANCE AS WELL AS THE MEDIAN ERROR FOR POSES ON THE DATASET $\mathcal{D}_{\text{Test}}^{\text{Real}}$. THE SIZE OF THE EMBEDDING E_i IS REPORTED IN BYTES.

S	F	Mem	Invisible Filtered		Invisible		Visible	
256	48	24 kB	61 cm	6.8°	97 cm	7.9°	33 cm	5.8°
128	96	24 kB	55 cm	7.7°	97 cm	7.4°	32 cm	5.6°
128	48	12 kB	67 cm	9.9°	113 cm	9.6°	29 cm	5.7°
128	24	6 kB	83 cm	11.2°	112 cm	9.7°	31 cm	5.7°
64	48	6 kB	81 cm	9.4°	119 cm	10.8°	36 cm	6.3°
1	3072	6 kB	123 cm	25.7°	122 cm	25.8°	93 cm	138.2°
1	348	696 B	150 cm	164.1°	135 cm	37.9°	80 cm	11.1°

model to reject pose estimations with high uncertainty based on a threshold computed with the Youden’s index [66].

Results: Evaluation on the real-world dataset $\mathcal{D}_{\text{Test}}^{\text{Real}}$ focuses on position and rotation accuracy, excluding quantitative BEV performance due to unavailable ground truth data.

We first report results similar to Tab. I on $\mathcal{D}_{\text{Test}}^{\text{Real}}$ in Tab. III. The results are in line with the results reported for $\mathcal{D}_{\text{Test}}^{\text{Sim}}$, with a distinct correlation between the number of patches S and features F and the performance of pose estimation. Notably, the performance in estimating rotations does not significantly vary between visible and invisible samples, demonstrating our model’s capability to robustly estimate poses without necessitating FOV overlap. The model exhibiting the highest accuracy achieves a median localization error of 97 cm and 7.9° for invisible samples, and 33 cm and 5.8° for visible samples. Note that the samples in the dataset $\mathcal{D}_{\text{Test}}^{\text{Real}}$ are at most 2 m apart, but the pose prediction is three-dimensional, resulting in a worst-case error of up to 4 m.

In all further evaluations, we detail the outcomes for the model configuration with $S = 128$ and $F = 48$. This model was selected for its balanced trade-off between BEV and pose estimation accuracy and manageable embedding size.

We investigate the efficiency of the uncertainty estimation as well as the distributions of pose errors more closely. Fig. 5 illustrates the distributions of position and rotation errors, along with the predicted variances over the angle difference between robot pairs in the dataset $\mathcal{D}_{\text{Test}}^{\text{Sim}}$. An angle difference of 0° signifies robots facing the same direction, potentially resulting in significant image overlap, while an angle difference of 180° indicates opposite directions, with no overlap. The Field Of View (FOV) overlap threshold is highlighted in red, delineating errors with overlap (below the line) from those

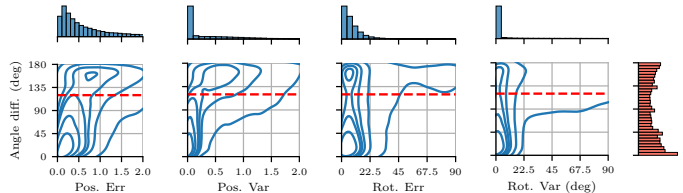


Fig. 5. We show qualitative distributions for position and rotation errors and variances over the relative angle between two robots on all edges of the real-world testset $\mathcal{D}_{\text{Test}}^{\text{Real}}$, containing 84048 unique edges. Two agents facing the same direction would have an angle difference of 0°, whereas two agents facing the opposite direction would have an angle difference of 180°. We show the FOV as dashed line, where any results below the line indicate that the edge has some image overlap and above no image overlap. The horizontal marginals show the distribution of each individual plot while the vertical marginal shows the distribution of angle differences over the testset. Note that the angle distribution is not uniform due to the real-world dataset collection where at least two cameras always face the opposite direction.

without (above the line). The analysis reveals that position errors remain consistent up to the FOV threshold, beyond which they escalate, as reflected in the predicted position variance. Conversely, rotation errors stay uniform across angle differences, with only a marginal increase for higher angles, though the predicted rotation variance notably rises.

These findings demonstrate our model’s capability to reliably estimate poses, even with minimal overlap, and to accurately predict higher variances under such conditions. We attribute this performance to the robust representational ability of the DinoV2 encoder and vision transformer models at large. The model appears to go beyond mere feature matching, instead achieving a sophisticated scene understanding that allows it to “imagine” unseen scene portions based on learned data priors, thereby facilitating pose estimation.

In Tab. IV, we investigate the performance of our model across the different scenes in the testing dataset $\mathcal{D}_{\text{Test}}^{\text{Real}}$. We provide a detailed breakdown of the median pose error for Invisible, Invisible Filtered and Visible cases for each of the eight scenes. While the pose error for visible samples is consistently between 22 cm/5.2° and 48 cm/7.5°, there are more outliers for invisible samples. This is due to some scenes having more or less symmetry, thus making it more challenging for the model to accurately predict poses. The pose prediction for the outdoor scene are least accurate, which is to be expected since the model was trained on indoor scenes. The Sunny scene has severe shadows and direct sunlight, while still providing low pose errors. The pose predictions are useful in all scenarios, demonstrating impressive generalization ability

TABLE IV
THE MEDIAN POSE ESTIMATION ERROR OF OUR MODEL ON EACH OF THE EIGHT $\mathcal{D}_{\text{Test}}^{\text{Real}}$ SCENES.

Scenario	Invisible		Invisible Filtered		Visible	
Corridor A	138 cm	129.6°	90 cm	11.4°	22 cm	5.2°
Corridor B	112 cm	5.9°	261 cm	8.2°	31 cm	5.2°
Office A	86 cm	14.4°	38 cm	9.6°	33 cm	7.5°
Office B	146 cm	10.4°	248 cm	4.6°	20 cm	4.7°
Outdoor	134 cm	9.5°	193 cm	28.7°	49 cm	6.9°
Study A	132 cm	6.7°	40 cm	5.1°	28 cm	5.3°
Study B	115 cm	8.9°	56 cm	9.6°	34 cm	5.5°
Sunny	77 cm	9.3°	49 cm	8.7°	22 cm	6.0°

TABLE V
WE SHOW MEDIAN POSE PREDICTION ERRORS FOR DIFFERENT DISTANCE THRESHOLDS d ON THE DATASET $\mathcal{D}_{\text{Test}}^{\text{Real}}$.

d	Invisible		Invisible Filtered		Visible	
<0.4 m	76 cm	7.6°	34 cm	6.7°	12 cm	4.9°
<0.8 m	80 cm	8.8°	48 cm	8.6°	21 cm	5.2°
<1.2 m	95 cm	9.5°	56 cm	8.5°	31 cm	5.8°
<1.6 m	123 cm	10.6°	97 cm	12.9°	45 cm	6.0°
<2.0 m	153 cm	10.5°	134 cm	16.2°	65 cm	6.8°

across a wide range of scenes.

Next, we evaluate the magnitude of pose prediction errors over different thresholds of distances between image pairs in Tab. V. We consider five bands of distances separated in 0.4 m chunks, ranging up to 2m. Note that the worst-case pose error is $2 \cdot d$ due to the three-dimensional pose predictions. While the error increases with an increasing distance between samples, the rotational error in particular stays low, and the position errors stay useful, ranging from 12 cm to 65 cm for visible samples, 34 cm to 134 cm for invisible filtered samples (samples that are not visible but for which the model predicts a high confidence) and 76 cm to 153 cm for all invisible samples.

We provide a qualitative sample in Fig. 6, where additionally to the simulation sample in Fig. 2, we also visualize the prediction uncertainty. More samples can be found in the supplementary material.

Finally, we conducted a baseline comparison with two feature-matching-based approaches, as summarized in Table VI. Both baseline methods extract and match features across two images to estimate the essential matrix, from which a rotation and a scale-less translation vector are derived. The first baseline employs OpenCV for ORB feature extraction followed by a brute-force matching technique. The second baseline, LightGlue, utilizes a neural network-based approach for feature extraction and matching. Given that both baselines estimate scale-less transformations, we adopted the same metric as used in LightGlue [23]. This metric computes the AUC at thresholds of 20, 45, and 90 degrees based on the maximum error in rotation and translation. Our findings indicate that our model surpasses both baselines in terms of performance across image pairs with and without visual overlap. It is important to note that while both baselines necessitate visual overlap to function effectively, our approach does not require

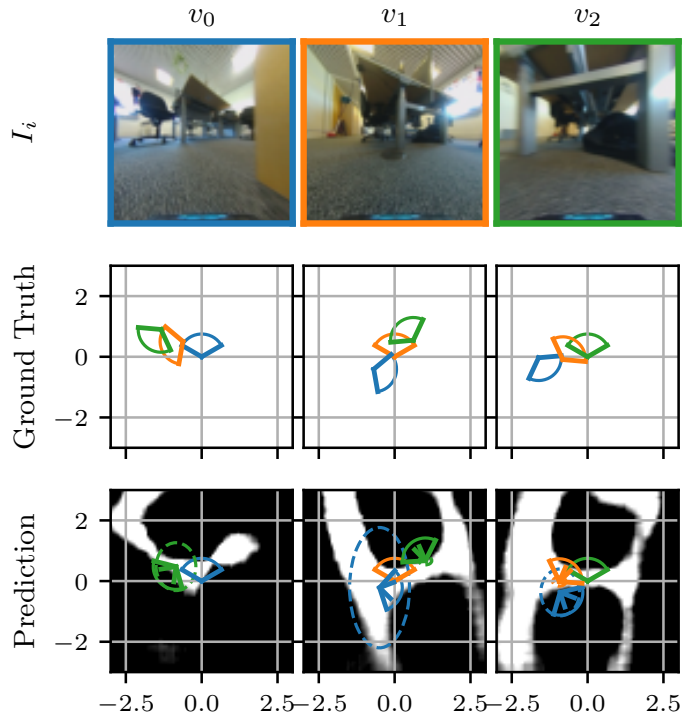


Fig. 6. By leveraging priors, such as the way humans lay out their rooms, our model can still provide rough relative position *even without overlapping fields of view*. This is generally impossible to do using classical approaches. We visualize a sample from our custom real-world testset $\mathcal{D}_{\text{Test}}^{\text{Real}}$ for three nodes, similar to the simulation sample in Fig. 2. We do not show the ground-truth BEV segmentation since we do not have labels for this. Additionally to the pose predictions $\hat{\mathbf{p}}_{i,ij}$, $\hat{\mathbf{R}}_{i,ij}$, we also visualize the predicted uncertainties σ_{ij}^2 .

TABLE VI
WE REPORT THE AUC METRIC AT 20, 45 AND 90° ON A FIRST-PRINCIPLES OPENCV AND AN NN-BASED BASELINE. WE REPORT THE AUC METRIC AT 20, 45 AND 90 DEGREE.

AUC@	Invisible			Visible		
	20	45	90	20	45	90
ORB/OpenCV [42]	0.16	1.60	7.43	9.41	21.92	38.03
LightGlue [23]	0.02	0.09	0.31	23.94	39.82	55.14
Ours	9.22	24.40	45.74	32.74	58.53	76.01

such overlap, highlighting its robustness and applicability in a broader range of scenarios.

C. Real-World Pose Control

In this section, we describe our real-world (online) multi-robot control experiment setup, including model deployment, wireless communication strategies, controllers, and results reported in Fig. 7, Fig. 8, Tab. VIII and Tab. VII.

Model deployment: We deploy a GNN-based model, selecting $F = 24$ and $S = 128$ for its balance between embedding size and performance, as reported in Tab. III. After training centralized in PyTorch, we compile f_{enc} , f_{pose} , and f_{agg} for decentralized deployment. Using TensorRT, a proprietary NVidia tool for ahead-of-time compilation of neural networks, we achieve sub-50 ms processing times. We benchmark the

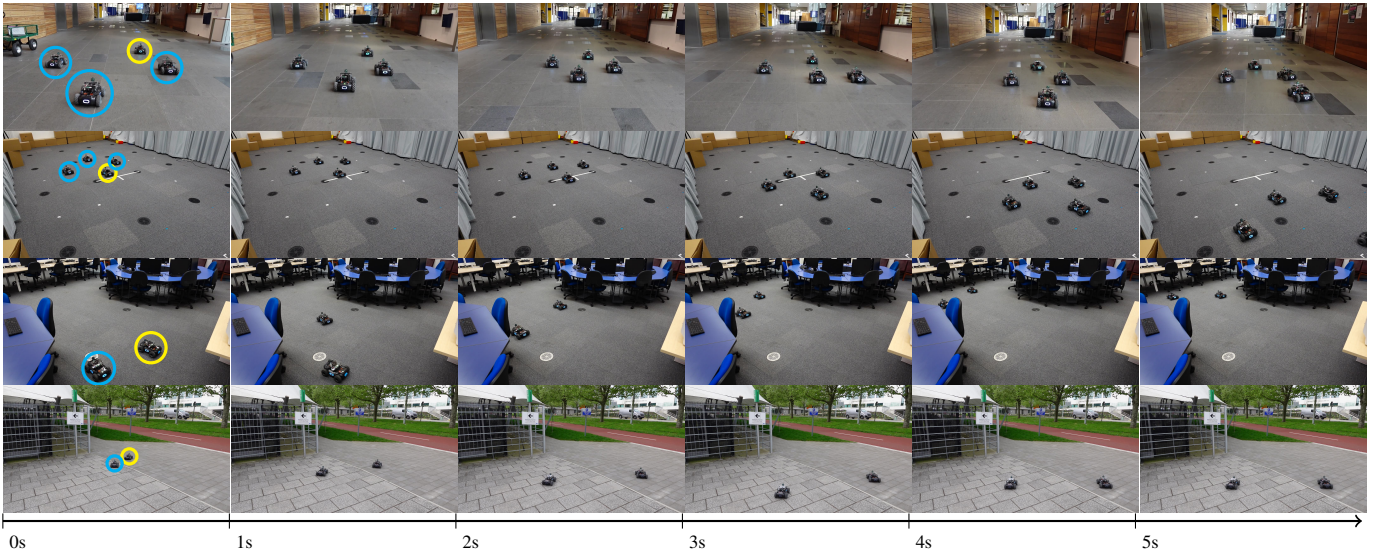


Fig. 7. We show snapshots of real-world deployments in different scenes with up to four robots. Each row contains six frames from a video recording, each spaced 1 s in time. We indicate the positions of the robots in the first frame, where the leader is circled yellow and the followers blue. The first three samples show indoor scenes, and the bottom sample is an outdoor deployment.

TABLE VII

WE REPORT THE MEAN AND ABSOLUTE TRACKING ERROR FOR BOTH LEADERS FOR ALL THREE TRAJECTORIES, AS WELL AS AVERAGE VELOCITIES. THE ERRORS ARE CONSISTENT WITH THE RESULTS REPORTED IN TAB. III.

Trajectory	Robot	Mean Abs.	Median	Vel
Fig. 8 dyn.	A	38 cm, 5.6°	38 cm, 4.8°	0.59 m/s
	B	28 cm, 5.1°	25 cm, 4.7°	0.58 m/s
Fig. 8 stat.	A	51 cm, 5.2°	48 cm, 5.3°	0.60 m/s
	B	28 cm, 5.6°	26 cm, 5.4°	0.61 m/s
Rect. dyn.	A	41 cm, 4.4°	42 cm, 4.4°	0.32 m/s
	B	29 cm, 5.1°	27 cm, 5.1°	0.81 m/s

runtime performance of the model on the Jetson Orin NX in Tab. VIII by averaging 100 sequential forward passes. We compare 16-bit and 32-bit float evaluated on the GPU or CPU and compilation with TensorRT. The model f_{enc} , generating the communicated embedding \mathbf{E}_i , has a total of 30 M parameters, and takes ca. 20 ms for one forward pass as FP16 optimized with Torch TensorRT on the GPU. This is $50\times$ faster than running the same model on the CPU. We also note that changing from 32-bit floats to 16-bit floats results in a $2.75\times$ speedup. The model f_{pose} , processing a pair of embeddings into a relative pose, has a total of 6 M parameters and takes ca. 4 ms for one forward pass. The model is run in a custom C++ environment integrated with ROS2 Humble and an ad-hoc WiFi network for inter-node communication to communicate image embeddings \mathbf{E}_i , achieving a 15 Hz processing rate for the whole pipeline, including image pre-processing, model evaluation, communication and pose prediction.

Ad-hoc WiFi: Image embeddings are sent between nodes at a rate of 15hz, with each being just over 6KiB. The fully distributed nature of our system matches well with a broad-

TABLE VIII

MODEL RUNTIME EVALUATION FOR $S = 128$ AND $F = 24$.

Type	Mode	Dev.	f_{enc}		f_{pose}	
FP16	TRT	GPU	19.22 ms	± 0.92 ms	4.15 ms	± 0.49 ms
FP16	JIT	GPU	36.79 ms	± 1.33 ms	8.04 ms	± 0.73 ms
FP32	JIT	GPU	99.32 ms	± 1.56 ms	13.57 ms	± 1.10 ms
FP32	JIT	CPU	952.04 ms	± 116.72 ms	248.41 ms	± 45.98 ms

cast communications topology, which theoretically can permit operation at scale. Broadcast messaging has a significant drawback, however, in that modern wireless data networking standards (IEEE 802.11/WiFi) fallback to very low bit rates to ensure maximum reception probability.

802.11 uses low bit rates for broadcast due to a lack of acknowledgment messages, which are the typical feedback mechanism for data rate control and retransmissions. The probability of a frame being lost due to the underlying CSMA/CA frame scheduler is non-trivial (3%+); a condition which worsens with increasing participating network nodes.

A higher level system, such as ROS2 communications middleware package CycloneDDS, can manage retransmissions, however currently available systems are not well suited to the requirements of a decentralized robotic network. In particular, they cannot detect network overload conditions, which can result in retransmissions that further load the network; finally resulting in a rapid increase in packet loss rates which renders the network as a whole unusable. While it is possible to tune such communications packages manually, the best parameter values are sensitive to highly variable deployment configuration parameters including ambient wireless network traffic. Manual tuning of network hardware, such as forcing increased broadcast bit rates, can alleviate this problem but is generally not as resilient at scale.

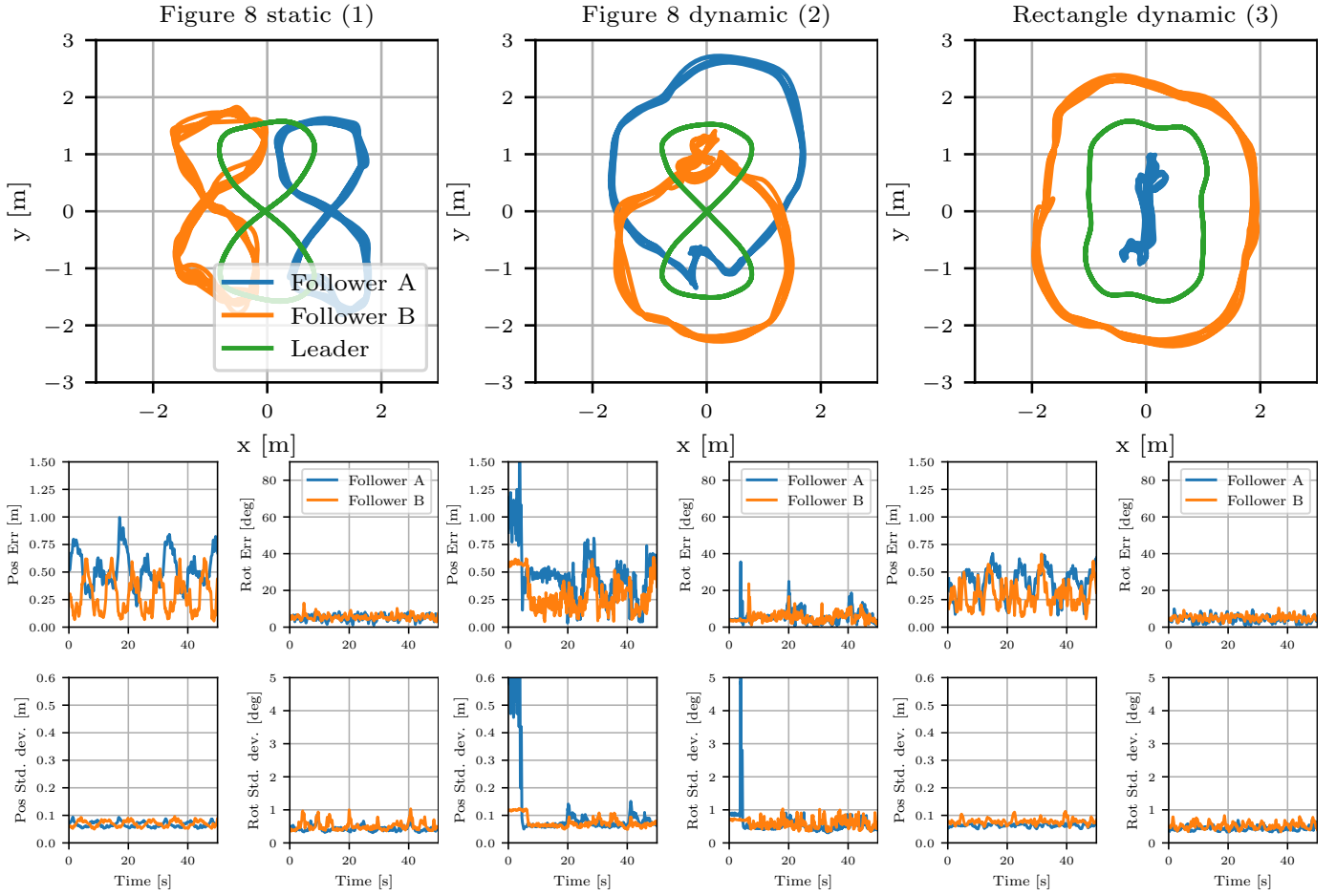


Fig. 8. We evaluate the tracking performance of our model and uncertainty-aware controller on three reference trajectories, with two follower robots (in blue and orange), positioned left and right of the leader robot (in green). For each trajectory, we report the tracking performance over time for position and rotation, as well as the predicted uncertainties. The left trajectory (1) is a Figure Eight with the leader always facing in the same direction. The middle trajectory (2) is similar to the first, but the leader is always facing the direction it is moving. In this trajectory, Follower A starts facing the opposite direction of the leader, resulting in high position variance and low rotation variance, which decreases as the robot rotates, facing the same direction as the leader. A spurious erroneous rotation prediction is accompanied by a high uncertainty. Note that as the leader moves through the trajectory, there is always one inside and one outside follower robot. This role changes depending on the section of the figure, resulting in these follower trajectories. The right trajectory (3) is a rounded rectangle. We show the trajectory for 120 s and the tracking error for the first 60 s. The tracking performance is consistent across multiple runs.

Our custom messaging protocol includes the ability to dynamically backoff messaging load based upon detected network conditions. Our system is also uses a shared slot TDMA message scheduling system which works with the 802.11 frame scheduler to maximize frame reception probability without compromising overall data rates.

Uncertainty-aware relative pose control: We utilize a PD controller for relative pose control of follower robots, implementing independent controllers for position and orientation. The controllers adjust based on the predicted uncertainty, deactivating if uncertainty exceeds certain thresholds to prevent inaccurate operations. This ensures that even with unreliable pose estimates, the robot can maintain its orientation toward the leader until a reliable estimate becomes available.

Experiment: We conduct qualitative experiments in a wide range of different environments, including outdoor, and quantitative experiments in a large room equipped with a motion capture system for accurate pose tracking. Two follower robots

are programmed to maintain a fixed distance of 0.6 m from a leader robot executing predefined trajectories. For the quantitative experiments, we assess the system’s tracking accuracy by comparing the ground truth and estimated relative poses, focusing on position and rotation errors and the predicted uncertainties for each dimension, using the same metrics introduced in Sec. V. Our model computes one uncertainty per 3D dimension, which we report as mean.

The three trajectories are two Figure Eight trajectory, one for which we keep the orientation of the leader constant, and one for which the leader is always facing in the direction it is moving. The third trajectory is a rounded rectangle, again with the leader facing the direction it is moving.

Results: Fig. 7 shows snapshots from four different real-world deployments, and Fig. 8 shows the trajectories of all robots for all quantitative experiments, as well as a visualization of the position and rotation error over time. We provide additional snapshots from more real-world experiments in the

appendix.

The qualitative experiments show a robust system that generalizes to a wide range of scenarios, including outdoors, albeit the scale prediction is less reliable in outdoor settings. Our model was trained exclusively on indoor data and generalizes to outdoor data due to the wide range of training data used on the DinoV2 encoder. The performance can be significantly improved by training on outdoor samples.

The tracking error in the quantitative experiments oscillates throughout the trajectories as the followers reactively adjust their position to the movements of the leader. Additionally, Figure 8 dynamic starts with Follower A facing the opposite direction of the Leader, resulting in higher position error and uncertainty while the rotation error is low. As the Follower rotates, the position uncertainty decreases. During this process, the model generates an erroneous rotation prediction that is accompanied with a spike in the uncertainty prediction. We note that the tracking error for Figure 8 static differs between both agents. This is due to the lack of structure in the lab environment and it affects both robots differently, resulting in better tracking performance for Follower A. The tracking error is consistent for the other trajectories. Tab. VII reports quantitative evaluations for the same results, which are in line with the results reported in Tab. III. Note that the velocities reported are average velocities of the follower robots. The velocities are consistent for both Figure 8 trajectories, but differ for the rectangle trajectory, as the inner robot moves more slowly than the outer robot.

VI. CONCLUSION

In this work, we introduced a novel visual spatial foundation model for multi-robot control applications, based on an existing computer vision foundation model. From monocular camera images, our model outputs accurate relative pose estimates and BEVs in the local frame by aggregating information from other robots. We validated our model on a custom real-world testset collected in various locations of an indoor office building. Then, we deployed our model onto robots, demonstrating real-time multi-robot control. We find that our model can accurately predict poses, even when there are no pixel-level correspondences, and correctly predict BEVs for obscured regions. In the real-world, we demonstrate accurate trajectory tracking, paving the way for more complex vision-only robotics tasks. Our model is able to estimate relative poses with a median pose error of up to 33 cm and 5.8° for visible edges and 97 cm and 5.9° for invisible edges on our real-world dataset containing 84048 relative poses. This is roughly equivalent to one body length of our robot. Using these estimated poses, our model increases the BEV prediction score by 8.75% compared to a multi-node aggregation scheme without poses.

In future work, we plan to investigate how to apply this model for other downstream tasks, and in combination with learning-based multi-agent control policies.

ACKNOWLEDGMENTS

This work was supported in part by European Research Council (ERC) Project 949949 (gAIA). J. Blumenkamp acknowledges the support of the ‘Studienstiftung des deutschen Volkes’ and an EPSRC tuition fee grant. We also acknowledge a gift from Arm.

REFERENCES

- [1] Yehya Abouelnaga, Mai Bui, and Slobodan Ilic. Distill-Pose: Lightweight Camera Localization Using Auxiliary Learning. In *2021 IEEE/RSJ International Conference on Intelligent Robots and Systems (IROS)*, pages 7919–7924, 2021. doi: 10.1109/IROS51168.2021.9635870. URL <https://ieeexplore.ieee.org/document/9635870>.
- [2] Javier Alonso-Mora, Ross Knepper, Roland Siegwart, and Daniela Rus. Local motion planning for collaborative multi-robot manipulation of deformable objects. In *2015 IEEE International Conference on Robotics and Automation (ICRA)*, pages 5495–5502, 2015. doi: 10.1109/ICRA.2015.7139967.
- [3] Eduardo Arnold, Jamie Wynn, Sara Vicente, Guillermo Garcia-Hernando, Áron Monszpart, Victor Adrian Prisacariu, Daniyar Turmukhambetov, and Eric Brachmann. Map-free Visual Relocalization: Metric Pose Relative to a Single Image. In *ECCV*, 2022. URL https://dl.acm.org/doi/10.1007/978-3-031-19769-7_40.
- [4] Matteo Bettini, Ajay Shankar, and Amanda Prorok. Heterogeneous Multi-Robot Reinforcement Learning. In *Proceedings of the 2023 International Conference on Autonomous Agents and Multiagent Systems, AAMAS '23*, page 1485–1494, Richland, SC, 2023. International Foundation for Autonomous Agents and Multiagent Systems. ISBN 9781450394321. URL <https://dl.acm.org/doi/abs/10.5555/3545946.3598801>.
- [5] Jan Blumenkamp, Steven Morad, Jennifer Gielis, Qingbiao Li, and Amanda Prorok. A Framework for Real-World Multi-Robot Systems Running Decentralized GNN-Based Policies. In *2022 International Conference on Robotics and Automation (ICRA)*, pages 8772–8778, 2022. doi: 10.1109/ICRA46639.2022.9811744. URL <https://ieeexplore.ieee.org/document/9811744>.
- [6] Ruojin Cai, Bharath Hariharan, Noah Snavely, and Hadar Averbuch-Elor. Extreme Rotation Estimation using Dense Correlation Volumes. In *IEEE/CVF Conference on Computer Vision and Pattern Recognition (CVPR)*, 2021. URL https://openaccess.thecvf.com/content/CVPR2021/html/Cai_Extreme_Rotation_Estimation_Using_Dense_Correlation_Volumes_CVPR_2021_paper.html.
- [7] Carlos Campos, Richard Elvira, Juan J. Gómez Rodríguez, José M. M. Montiel, and Juan D. Tardós. ORB-SLAM3: An Accurate Open-Source Library for Visual, Visual-Inertial, and Multimap SLAM. *IEEE Transactions on Robotics*, 37(6):1874–1890, 2021. doi: 10.1109/TRO.2021.3075644. URL <https://ieeexplore.ieee.org/abstract/document/9440682>.

- [8] Oscar De Silva, George K. I. Mann, and Raymond G. Gosine. An Ultrasonic and Vision-Based Relative Positioning Sensor for Multirobot Localization. *IEEE Sensors Journal*, 15(3):1716–1726, 2015. doi: 10.1109/JSEN.2014.2364684. URL <https://ieeexplore.ieee.org/abstract/document/6934978>.
- [9] Jia Deng, Wei Dong, Richard Socher, Li-Jia Li, Kai Li, and Li Fei-Fei. ImageNet: A large-scale hierarchical image database. In *2009 IEEE Conference on Computer Vision and Pattern Recognition*, pages 248–255, 2009. doi: 10.1109/CVPR.2009.5206848. URL <https://ieeexplore.ieee.org/document/5206848>.
- [10] Alexey Dosovitskiy, Lucas Beyer, Alexander Kolesnikov, Dirk Weissenborn, Xiaohua Zhai, Thomas Unterthiner, Mostafa Dehghani, Matthias Minderer, Georg Heigold, Sylvain Gelly, Jakob Uszkoreit, and Neil Houlsby. An Image is Worth 16x16 Words: Transformers for Image Recognition at Scale. In *International Conference on Learning Representations*, 2021. URL <https://openreview.net/forum?id=YicbFdNTTy>.
- [11] Prमित Dutta, Ganesh Sistu, Senthil Yogamani, Edgar Galván, and John McDonald. ViT-BEVSeg: A Hierarchical Transformer Network for Monocular Birds-Eye-View Segmentation. In *2022 International Joint Conference on Neural Networks (IJCNN)*, pages 1–7, 2022. doi: 10.1109/IJCNN55064.2022.9891987. URL <https://ieeexplore.ieee.org/document/9891987>.
- [12] Sovann En, Alexis Lechervy, and Frédéric Jurie. RP-Net: an End-to-End Network for Relative Camera Pose Estimation. In *Proceedings of the European Conference on Computer Vision (ECCV) Workshops*, 2018. URL https://link.springer.com/chapter/10.1007/978-3-030-11009-3_46.
- [13] Yarin Gal and Zoubin Ghahramani. Dropout as a Bayesian Approximation: Representing Model Uncertainty in Deep Learning. In Maria Florina Balcan and Kilian Q. Weinberger, editors, *Proceedings of The 33rd International Conference on Machine Learning*, volume 48 of *Proceedings of Machine Learning Research*, pages 1050–1059, New York, New York, USA, 20–22 Jun 2016. PMLR. URL <https://proceedings.mlr.press/v48/gal16.html>.
- [14] Fernando Gama, Ekaterina Tolstaya, and Alejandro Ribeiro. Graph Neural Networks for Decentralized Controllers. In *ICASSP 2021 - 2021 IEEE International Conference on Acoustics, Speech and Signal Processing (ICASSP)*, pages 5260–5264, 2021. doi: 10.1109/ICASSP39728.2021.9414563. URL <https://ieeexplore.ieee.org/document/9414563>.
- [15] Fernando Gama, Qingbiao Li, Ekaterina Tolstaya, Amanda Prorok, and Alejandro Ribeiro. Synthesizing Decentralized Controllers With Graph Neural Networks and Imitation Learning. *IEEE Transactions on Signal Processing*, 70:1932–1946, 2022. doi: 10.1109/TSP.2022.3166401. URL <https://ieeexplore.ieee.org/document/9755021>.
- [16] Yushan Han, Hui Zhang, Huifang Li, Yi Jin, Congyan Lang, and Yidong Li. Collaborative Perception in Autonomous Driving: Methods, Datasets, and Challenges. *IEEE Intelligent Transportation Systems Magazine*, 15(6):131–151, 2023. doi: 10.1109/MITS.2023.3298534. URL <https://ieeexplore.ieee.org/document/10248946>.
- [17] Alex Kendall and Yarin Gal. What Uncertainties Do We Need in Bayesian Deep Learning for Computer Vision? In I. Guyon, U. Von Luxburg, S. Bengio, H. Wallach, R. Fergus, S. Vishwanathan, and R. Garnett, editors, *Advances in Neural Information Processing Systems*, volume 30. Curran Associates, Inc., 2017. URL https://papers.nips.cc/paper_files/paper/2017/hash/2650d6089a6d640c5e85b2b88265dc2b-Abstract.html.
- [18] Alex Kendall, Matthew Grimes, and Roberto Cipolla. PoseNet: A Convolutional Network for Real-Time 6-DOF Camera Relocalization. In *Proceedings of the IEEE International Conference on Computer Vision (ICCV)*, December 2015. URL https://openaccess.thecvf.com/content_iccv_2015/html/Kendall_PoseNet_A_Convolutional_ICCV_2015_paper.html.
- [19] Balaji Lakshminarayanan, Alexander Pritzel, and Charles Blundell. Simple and Scalable Predictive Uncertainty Estimation using Deep Ensembles. In I. Guyon, U. Von Luxburg, S. Bengio, H. Wallach, R. Fergus, S. Vishwanathan, and R. Garnett, editors, *Advances in Neural Information Processing Systems*, volume 30. Curran Associates, Inc., 2017. URL https://papers.nips.cc/paper_files/paper/2017/hash/9ef2ed4b7fd2c810847ffa5fa85bce38-Abstract.html.
- [20] Zakaria Laskar, Iaroslav Melekhov, Surya Kalia, and Juho Kannala. Camera Relocalization by Computing Pairwise Relative Poses Using Convolutional Neural Network. In *The IEEE International Conference on Computer Vision (ICCV)*, Oct 2017. URL <https://github.com/AaltoVision/camera-relocalisation>.
- [21] Yiming Li, Dekun Ma, Ziyang An, Zixun Wang, Yiqi Zhong, Siheng Chen, and Chen Feng. V2X-Sim: Multi-Agent Collaborative Perception Dataset and Benchmark for Autonomous Driving. *IEEE Robotics and Automation Letters*, 7(4):10914–10921, 2022. doi: 10.1109/LRA.2022.3192802. URL <https://ieeexplore.ieee.org/document/9835036>.
- [22] Yiming Li, Juexiao Zhang, Dekun Ma, Yue Wang, and Chen Feng. Multi-Robot Scene Completion: Towards Task-Agnostic Collaborative Perception. In Karen Liu, Dana Kulic, and Jeff Ichnowski, editors, *Proceedings of The 6th Conference on Robot Learning*, volume 205 of *Proceedings of Machine Learning Research*, pages 2062–2072. PMLR, 14–18 Dec 2023. URL <https://proceedings.mlr.press/v205/li23e.html>.
- [23] Philipp Lindenberger, Paul-Edouard Sarlin, and Marc Pollefeys. LightGlue: Local Feature Matching at Light Speed. In *Proceedings of the IEEE/CVF International Conference on Computer Vision (ICCV)*, pages 17627–17638, October 2023. URL

- https://openaccess.thecvf.com/content/ICCV2023/html/Lindenberger_LightGlue_Local_Feature_Matching_at_Light_Speed_ICCV_2023_paper.html.
- [24] Yingfei Liu, Junjie Yan, Fan Jia, Shuailin Li, Aqi Gao, Tiancai Wang, and Xiangyu Zhang. PETRv2: A Unified Framework for 3D Perception from Multi-Camera Images. In *Proceedings of the IEEE/CVF International Conference on Computer Vision (ICCV)*, pages 3262–3272, October 2023. URL https://openaccess.thecvf.com/content/ICCV2023/html/Liu_PETRv2_A_Unified_Framework_for_3D_Perception_from_Multi-Camera_Images_ICCV_2023_paper.html.
- [25] David G Lowe. Distinctive image features from scale-invariant keypoints. *International journal of computer vision*, 60:91–110, 2004. URL <https://link.springer.com/article/10.1023/B:VISI.0000029664.99615.94>.
- [26] Alcherio Martinoli, Kjerstin Easton, and William Agassounon. Modeling swarm robotic systems: A case study in collaborative distributed manipulation. *The International Journal of Robotics Research*, 23(4-5):415–436, 2004.
- [27] Iaroslav Melekhov, Juha Ylioinas, Juho Kannala, and Esa Rahtu. Relative Camera Pose Estimation Using Convolutional Neural Networks. In Jacques Blanc-Talon, Rudi Penne, Wilfried Philips, Dan Popescu, and Paul Scheunders, editors, *Advanced Concepts for Intelligent Vision Systems*, pages 675–687, Cham, 2017. Springer International Publishing. ISBN 978-3-319-70353-4. URL https://link.springer.com/chapter/10.1007/978-3-319-70353-4_57.
- [28] Akmaral Moldagalieva and Wolfgang Hönig. Virtual Omnidirectional Perception for Downwash Prediction within a Team of Nano Multirotors Flying in Close Proximity, 2023. URL <https://arxiv.org/abs/2303.03898>.
- [29] Paola Torrico Morón, Sahar Salimpour, Lei Fu, Xianjia Yu, Jorge Peña Queraltá, and Tomi Westerlund. Benchmarking UWB-Based Infrastructure-Free Positioning and Multi-Robot Relative Localization: Dataset and Characterization, 2023. URL <https://arxiv.org/abs/2305.08532>.
- [30] D.A. Nix and A.S. Weigend. Estimating the mean and variance of the target probability distribution. In *Proceedings of 1994 IEEE International Conference on Neural Networks (ICNN'94)*, volume 1, pages 55–60 vol.1, 1994. doi: 10.1109/ICNN.1994.374138. URL <https://ieeexplore.ieee.org/document/374138>.
- [31] Kwang-Kyo Oh, Myoung-Chul Park, and Hyo-Sung Ahn. A survey of multi-agent formation control. *Automatica*, 53:424–440, 2015.
- [32] Maxime Oquab, Timothée Darcet, Theo Moutakanni, Huy V. Vo, Marc Szafraniec, Vasil Khalidov, Pierre Fernandez, Daniel Haziza, Francisco Massa, Alaaeldin El-Nouby, Russell Howes, Po-Yao Huang, Hu Xu, Vasu Sharma, Shang-Wen Li, Wojciech Galuba, Mike Rabbat, Mido Assran, Nicolas Ballas, Gabriel Synnaeve, Ishan Misra, Herve Jegou, Julien Mairal, Patrick Labatut, Armand Joulin, and Piotr Bojanowski. DINOv2: Learning Robust Visual Features without Supervision, 2023. URL <https://github.com/facebookresearch/dinov2/tree/main>.
- [33] Rémi Pautrat, Iago Suárez, Yifan Yu, Marc Pollefeys, and Viktor Larsson. GlueStick: Robust Image Matching by Sticking Points and Lines Together. In *Proceedings of the IEEE/CVF International Conference on Computer Vision (ICCV)*, pages 9706–9716, October 2023. URL https://openaccess.thecvf.com/content/ICCV2023/html/Pautrat_GlueStick_Robust_Image_Matching_by_Sticking_Points_and_Lines_Together_ICCV_2023_paper.html.
- [34] Lang Peng, Zhirong Chen, Zhangjie Fu, Pengpeng Liang, and Erkang Cheng. BEVSegFormer: Bird’s Eye View Semantic Segmentation From Arbitrary Camera Rigs. In *Proceedings of the IEEE/CVF Winter Conference on Applications of Computer Vision (WACV)*, pages 5935–5943, January 2023. URL https://openaccess.thecvf.com/content/WACV2023/html/Peng_BEVSegFormer_Birds_Eye_View_Semantic_Segmentation_From_Arbitrary_Camera_Rigs_WACV_2023_paper.html.
- [35] Valentin Peretroukhin, Matthew Giamou, W. Nicholas Greene, David Rosen, Jonathan Kelly, and Nicholas Roy. A Smooth Representation of Belief over SO(3) for Deep Rotation Learning with Uncertainty. In *Proceedings of Robotics: Science and Systems*, Corvallis, Oregon, USA, July 2020. doi: 10.15607/RSS.2020.XVI.007. URL <https://www.roboticsproceedings.org/rss16/p007.html>.
- [36] Jonah Philion and Sanja Fidler. Lift, Splat, Shoot: Encoding Images From Arbitrary Camera Rigs by Implicitly Unprojecting to 3D. In *Proceedings of the European Conference on Computer Vision*, 2020. URL https://dl.acm.org/doi/abs/10.1007/978-3-030-58568-6_12.
- [37] Praveen Kumar Rajendran, Sumit Mishra, Luiz Felipe Vecchietti, and Dongsoo Har. RelMobNet: End-to-End Relative Camera Pose Estimation Using a Robust Two-Stage Training. In Leonid Karlinsky, Tomer Michaeli, and Ko Nishino, editors, *Computer Vision – ECCV 2022 Workshops*, pages 238–252, Cham, 2023. Springer Nature Switzerland. ISBN 978-3-031-25075-0. URL https://link.springer.com/chapter/10.1007/978-3-031-25075-0_18.
- [38] Santhosh Kumar Ramakrishnan, Aaron Gokaslan, Erik Wijmans, Oleksandr Maksymets, Alexander Clegg, John M Turner, Eric Undersander, Wojciech Galuba, Andrew Westbury, Angel X Chang, Manolis Savva, Yili Zhao, and Dhruv Batra. Habitat-Matterport 3D Dataset (HM3D): 1000 Large-scale 3D Environments for Embodied AI. In *Thirty-fifth Conference on Neural Information Processing Systems Datasets and Benchmarks Track*, 2021. URL <https://aihabitat.org/datasets/hm3d>.
- [39] Craig W Reynolds. Flocks, herds and schools: A distributed behavioral model. In *Proceedings of the 14th annual conference on Computer graphics and interactive techniques*, pages 25–34, 1987.
- [40] Chris Rockwell, Justin Johnson, and David F. Fouhey. The 8-Point Algorithm as an Inductive Bias for Relative

- Pose Prediction by ViTs. In *2022 International Conference on 3D Vision (3DV)*, pages 1–11, 2022. doi: 10.1109/3DV57658.2022.00028. URL <https://ieeexplore.ieee.org/abstract/document/10044394>.
- [41] Thomas Roddick and Roberto Cipolla. Predicting Semantic Map Representations From Images Using Pyramid Occupancy Networks. In *Proceedings of the IEEE/CVF Conference on Computer Vision and Pattern Recognition (CVPR)*, June 2020. URL https://openaccess.thecvf.com/content_CVPR_2020/html/Roddick_Predicting_Semantic_Map_Representations_From_Images_Using_Pyramid_Occupancy_Networks_CVPR_2020_paper.html.
- [42] Ethan Rublee, Vincent Rabaud, Kurt Konolige, and Gary Bradski. Orb: An efficient alternative to sift or surf. In *2011 International Conference on Computer Vision*, pages 2564–2571, 2011. doi: 10.1109/ICCV.2011.6126544.
- [43] Xu Runsheng, Xiang Hao, Tu Zhengzhong, Xia Xin, Yang Ming-Hsuan, and Ma Jiaqi. V2X-ViT: Vehicle-to-Everything Cooperative Perception with Vision Transformer. In *Proceedings of the European Conference on Computer Vision (ECCV)*, 2022. URL https://dl.acm.org/doi/abs/10.1007/978-3-031-19842-7_7.
- [44] Paul-Edouard Sarlin, Daniel DeTone, Tomasz Malisiewicz, and Andrew Rabinovich. SuperGlue: Learning Feature Matching With Graph Neural Networks. In *Proceedings of the IEEE/CVF Conference on Computer Vision and Pattern Recognition (CVPR)*, June 2020. URL https://openaccess.thecvf.com/content_CVPR_2020/html/Sarlin_SuperGlue_Learning_Feature_Matching_With_Graph_Neural_Networks_CVPR_2020_paper.html.
- [45] Paul-Edouard Sarlin, Ajaykumar Unagar, Mans Larsson, Hugo Germain, Carl Toft, Viktor Larsson, Marc Pollefeys, Vincent Lepetit, Lars Hammarstrand, Fredrik Kahl, and Torsten Sattler. Back to the Feature: Learning Robust Camera Localization From Pixels To Pose. In *Proceedings of the IEEE/CVF Conference on Computer Vision and Pattern Recognition (CVPR)*, pages 3247–3257, June 2021. URL https://openaccess.thecvf.com/content/CVPR2021/html/Sarlin_Back_to_the_Feature_Learning_Robust_Camera_Localization_From_Pixels_CVPR_2021_paper.html.
- [46] Martin Saska, Jan Vakula, and Libor Pěrućil. Swarms of micro aerial vehicles stabilized under a visual relative localization. In *2014 IEEE International Conference on Robotics and Automation (ICRA)*, pages 3570–3575, 2014. doi: 10.1109/ICRA.2014.6907374. URL <https://ieeexplore.ieee.org/abstract/document/6907374>.
- [47] Manolis Savva, Abhishek Kadian, Oleksandr Maksymets, Yili Zhao, Erik Wijmans, Bhavana Jain, Julian Straub, Jia Liu, Vladlen Koltun, Jitendra Malik, Devi Parikh, and Dhruv Batra. Habitat: A Platform for Embodied AI Research. In *Proceedings of the IEEE/CVF International Conference on Computer Vision (ICCV)*, 2019. URL https://openaccess.thecvf.com/content_ICCV_2019/html/Savva_Habitat_A_Platform_for_Embodied_AI_Research_ICCV_2019_paper.html.
- [48] Davide Scaramuzza and Friedrich Fraundorfer. Visual Odometry [Tutorial]. *IEEE Robotics & Automation Magazine*, 18(4):80–92, 2011. doi: 10.1109/MRA.2011.943233. URL <https://ieeexplore.ieee.org/abstract/document/6096039>.
- [49] Johannes L. Schönberger and Jan-Michael Frahm. Structure-from-Motion Revisited. In *2016 IEEE Conference on Computer Vision and Pattern Recognition (CVPR)*, pages 4104–4113, 2016. doi: 10.1109/CVPR.2016.445. URL <https://ieeexplore.ieee.org/abstract/document/7780814>.
- [50] Guni Sharon, Roni Stern, Ariel Felner, and Nathan R Sturtevant. Conflict-based search for optimal multi-agent pathfinding. *Artificial intelligence*, 219:40–66, 2015.
- [51] Stephen L. Smith, Mac Schwager, and Daniela Rus. Persistent robotic tasks: Monitoring and sweeping in changing environments. *IEEE Transactions on Robotics*, 28(2):410–426, 2012. doi: 10.1109/TRO.2011.2174493.
- [52] Carole H Sudre, Wenqi Li, Tom Vercauteren, Sebastien Ourselin, and M Jorge Cardoso. Generalised dice overlap as a deep learning loss function for highly unbalanced segmentations. In *Deep Learning in Medical Image Analysis and Multimodal Learning for Clinical Decision Support: Third International Workshop, DLMIA 2017, and 7th International Workshop, ML-CDS 2017, Held in Conjunction with MICCAI 2017, Québec City, QC, Canada, September 14, Proceedings 3*, pages 240–248. Springer, 2017. URL https://link.springer.com/chapter/10.1007/978-3-319-67558-9_28.
- [53] Jiaming Sun, Zehong Shen, Yuang Wang, Hujun Bao, and Xiaowei Zhou. LoFTR: Detector-Free Local Feature Matching With Transformers. In *Proceedings of the IEEE/CVF Conference on Computer Vision and Pattern Recognition (CVPR)*, pages 8922–8931, June 2021. URL https://openaccess.thecvf.com/content/CVPR2021/html/Sun_LoFTR_Detector-Free_Local_Feature_Matching_With_Transformers_CVPR_2021_paper.html.
- [54] Andrew Szot, Alex Clegg, Eric Undersander, Erik Wijmans, Yili Zhao, John Turner, Noah Maestre, Mustafa Mukadam, Devendra Chaplot, Oleksandr Maksymets, Aaron Gokaslan, Vladimir Vondrus, Sameer Dharur, Franziska Meier, Wojciech Galuba, Angel Chang, Zsolt Kira, Vladlen Koltun, Jitendra Malik, Manolis Savva, and Dhruv Batra. Habitat 2.0: Training Home Assistants to Rearrange their Habitat. In *Advances in Neural Information Processing Systems (NeurIPS)*, 2021. URL <https://proceedings.neurips.cc/paper/2021/hash/021bbc7ee20b71134d53e20206bd6feb-Abstract.html>.
- [55] Ekaterina Tolstaya, Fernando Gama, James Paulos, George Pappas, Vijay Kumar, and Alejandro Ribeiro. Learning Decentralized Controllers for Robot Swarms with Graph Neural Networks. In Leslie Pack Kaelbling, Danica Kragic, and Komei Sugiura, editors, *Proceed-*

- ings of the *Conference on Robot Learning*, volume 100 of *Proceedings of Machine Learning Research*, pages 671–682. PMLR, 30 Oct–01 Nov 2020. URL <https://proceedings.mlr.press/v100/tolstaya20a.html>.
- [56] Jur Van den Berg, Ming Lin, and Dinesh Manocha. Reciprocal velocity obstacles for real-time multi-agent navigation. In *2008 IEEE international conference on robotics and automation*, pages 1928–1935. Ieee, 2008.
- [57] Ashish Vaswani, Noam Shazeer, Niki Parmar, Jakob Uszkoreit, Llion Jones, Aidan N Gomez, Łukasz Kaiser, and Illia Polosukhin. Attention is All you Need. In I. Guyon, U. Von Luxburg, S. Bengio, H. Wallach, R. Fergus, S. Vishwanathan, and R. Garnett, editors, *Advances in Neural Information Processing Systems*, volume 30. Curran Associates, Inc., 2017. URL https://papers.nips.cc/paper_files/paper/2017/hash/3f5ee243547dee91fbd053c1c4a845aa-Abstract.html.
- [58] Viktor Walter, Martin Saska, and Antonio Franchi. Fast Mutual Relative Localization of UAVs using Ultraviolet LED Markers. In *2018 International Conference on Unmanned Aircraft Systems (ICUAS)*, pages 1217–1226, 2018. doi: 10.1109/ICUAS.2018.8453331. URL <https://ieeexplore.ieee.org/abstract/document/8453331>.
- [59] Tsun-Hsuan Wang, Sivabalan Manivasagam, Ming Liang, Bin Yang, Wenyuan Zeng, and Raquel Urtasun. V2VNet: Vehicle-to-Vehicle Communication for Joint Perception and Prediction. In Andrea Vedaldi, Horst Bischof, Thomas Brox, and Jan-Michael Frahm, editors, *Computer Vision – ECCV 2020*, pages 605–621, Cham, 2020. Springer International Publishing. ISBN 978-3-030-58536-5. URL https://link.springer.com/chapter/10.1007/978-3-030-58536-5_36.
- [60] Karl Weiss, Taghi M Khoshgoftaar, and DingDing Wang. A survey of transfer learning. *Journal of Big data*, 3:1–40, 2016.
- [61] Dominik Winkelbauer, Maximilian Denninger, and Rudolph Triebel. Learning to Localize in New Environments from Synthetic Training Data. In *2021 IEEE International Conference on Robotics and Automation (ICRA)*, pages 5840–5846, 2021. doi: 10.1109/ICRA48506.2021.9560872. URL <https://ieeexplore.ieee.org/document/9560872>.
- [62] Runsheng Xu, Zhengzhong Tu, Hao Xiang, Wei Shao, Bolei Zhou, and Jiaqi Ma. CoBEVT: Cooperative Bird’s Eye View Semantic Segmentation with Sparse Transformers. In Karen Liu, Dana Kulic, and Jeff Ichnowski, editors, *Proceedings of The 6th Conference on Robot Learning*, volume 205 of *Proceedings of Machine Learning Research*, pages 989–1000. PMLR, 14–18 Dec 2023. URL <https://proceedings.mlr.press/v205/xu23a.html>.
- [63] Chenhao Yang, Yuyi Liu, and Andreas Zell. RCPNet: Deep-Learning based Relative Camera Pose Estimation for UAVs. In *2020 International Conference on Unmanned Aircraft Systems (ICUAS)*, pages 1085–1092, 2020. doi: 10.1109/ICUAS48674.2020.9214000. URL <https://ieeexplore.ieee.org/abstract/document/9214000>.
- [64] Chenhao Yang, Yuyi Liu, and Andreas Zell. Learning-based Camera Relocalization with Domain Adaptation via Image-to-Image Translation. In *2021 International Conference on Unmanned Aircraft Systems (ICUAS)*, pages 1047–1054, 2021. doi: 10.1109/ICUAS51884.2021.9476673. URL <https://ieeexplore.ieee.org/abstract/document/9476673>.
- [65] Chenyu Yang, Yuntao Chen, Hao Tian, Chenxin Tao, Xizhou Zhu, Zhaoxiang Zhang, Gao Huang, Hongyang Li, Yu Qiao, Lewei Lu, Jie Zhou, and Jifeng Dai. BEVFormer v2: Adapting Modern Image Backbones to Bird’s-Eye-View Recognition via Perspective Supervision. In *Proceedings of the IEEE/CVF Conference on Computer Vision and Pattern Recognition (CVPR)*, pages 17830–17839, June 2023. URL https://openaccess.thecvf.com/content/CVPR2023/html/Yang_BEVFormer_v2_Adapting_Modern_Image_Backbones_to_Birds-Eye-View_Recognition_via_CVPR_2023_paper.html.
- [66] William J Youden. Index for rating diagnostic tests. *Cancer*, 3(1):32–35, 1950.
- [67] Alexander Zelinsky, Ray A Jarvis, JC Byrne, Shinichi Yuta, et al. Planning paths of complete coverage of an unstructured environment by a mobile robot. In *Proceedings of international conference on advanced robotics*, volume 13, pages 533–538. Citeseer, 1993.
- [68] Qunjie Zhou, Torsten Sattler, Marc Pollefeys, and Laura Leal-Taixé. To Learn or Not to Learn: Visual Localization from Essential Matrices. In *2020 IEEE International Conference on Robotics and Automation (ICRA)*, pages 3319–3326, 2020. doi: 10.1109/ICRA40945.2020.9196607. URL <https://ieeexplore.ieee.org/abstract/document/9196607>.
- [69] Yang Zhou, Jiuhong Xiao, Yue Zhou, and Giuseppe Loianno. Multi-Robot Collaborative Perception With Graph Neural Networks. *IEEE Robotics and Automation Letters*, 7(2):2289–2296, 2022. doi: 10.1109/LRA.2022.3141661. URL <https://ieeexplore.ieee.org/abstract/document/9676458>.

APPENDIX A TRAINING

A. Dataset

The samples of the datasets $\mathcal{D}_{\text{Train}}^{\text{Sim}}$, $\mathcal{D}_{\text{Test}}^{\text{Sim}}$ and $\mathcal{D}_{\text{Val}}^{\text{Sim}}$ are randomly sampled to be within orientation range $[-\frac{\pi}{32}, \frac{\pi}{32}]$ for roll and pitch, and within a height of 0.1 to 0.3 meters, representing the camera mounted on the robot.

B. Model architecture

This section introduces all hyperparameters and implementation details of the model architecture.

All transformer blocks have 12 attention heads. The MLP used in the transformer has a hidden size of $4F$. All blocks utilize a dropout of 0.2.

The encoder f_{enc} consists of the pre-trained DinoV2 vision transformer and two more transformer layers previously described as $f_{\text{trans}}^{\text{enc}}$. The input feature size is 224×224 , of which DinoV2 generates an embedding of size $S = 256$ and $F = 384$. We add a linear layer that transforms F down to the parameter described in this paper (e.g. 24) while maintaining S . The output of this is then cropped to the S described in this paper (e.g. 128) by cropping the sequence length at that position.

The pairwise pose encoder f_{pose} consists of transformer $f_{\text{trans}}^{\text{pose}}$, which is assembled from five transformer blocks, and four MLPs f_p^μ , f_p^σ , f_R^μ , f_R^σ . We first project the embedding \mathbf{E}_i to a larger feature size $F = 192$ using a linear layer. Each transformer layer has $F = 192$ in and out features. The learnable transformer positional embedding \mathbf{S}_{pose} is initialized to match F and S , with normal distribution initialization of $\sigma = 0.02$. The MLPs f_p^μ , f_p^σ , f_R^μ , f_R^σ are represented by one linear layer mapping the output of the transformer from $F = 192$ to $F = 17$ (position: 3, position uncertainty: 3, orientation: 10, orientation uncertainty: 1).

The feature aggregation function f_{agg} is built from $f_{\text{trans}}^{\text{agg}}$, which consists of five transformer layers, and $f_{\text{trans}}^{\text{post}}$, which consists of one transformer layer, all of which have an embedding size of $F = 192$. The MLP f_{aggpos} consists of three layers with 17, 48 and 48 neurons each, the positional embedding \mathbf{S}_{agg} is initialized similar to the one in f_{pose} , and the BEV decoder f_{BEV} takes the first sequence element of $f_{\text{trans}}^{\text{post}}$ as input and scales it up through seven alternations of convolutions and upsampling.

C. Loss function

The parameters α balances between Dice and BCE loss, and we set it to $\alpha = 0.5$, and the parameter β balances between position and orientation prediction accuracy, and we set it to 1, given equal weight to both.

D. Training

We set the initial learning rate to 1^{-5} and configure a learning rate schedule to increase this over two epochs up to 1^{-3} , followed by a sinusoidal decline to 0 over 20 epochs.

We show the train and validation loss for $N = 5$ training runs with different seeds in Fig. 9.

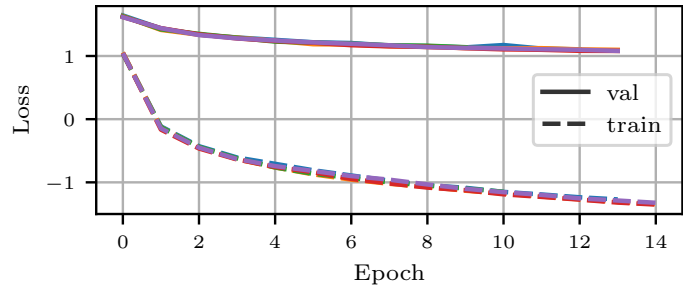


Fig. 9. We show the training and validation loss for a model trained with $F = 48$ and $S = 128$ over $N = 5$ different training seeds. We report a low average standard deviation of 0.011374 over all epochs on the validation loss.

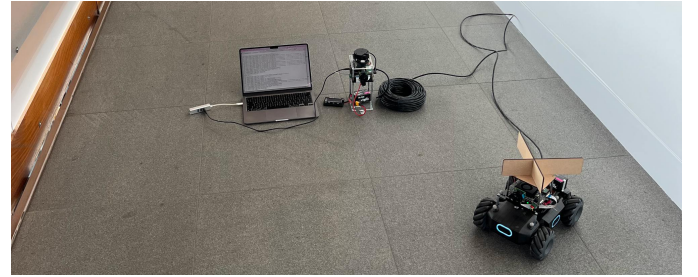


Fig. 10. To collect the real-world testset, we construct a static base station equipped with two cameras facing in opposite directions and a lidar. We add a marker on the robot so that its pose can be tracked with the lidar and then manually move the robot around the base station.

APPENDIX B REAL-WORLD DATASET

We visualize the five different scenes we collected the dataset from as well as the data distribution from each respective scene in Fig. 12. We explain the setup of our data collection unit in Fig. 10.

APPENDIX C RESULTS

We perform a further evaluation on the distributions of pose errors and variations on the simulation test set $\mathcal{D}_{\text{Test}}^{\text{Sim}}$ in Fig. 13. The results are in line with the results performed on $\mathcal{D}_{\text{Test}}^{\text{Real}}$ in the main manuscript.

A. Simulation

We visualize four additional samples from the simulation dataset $\mathcal{D}_{\text{Test}}^{\text{Sim}}$ in Fig. 14, Fig. 15, Fig. 16, Fig. 17, Fig. 18 and Fig. 19.

B. Real-World

We visualize two more samples from the real-world dataset $\mathcal{D}_{\text{Test}}^{\text{Real}}$ in Fig. 20, Fig. 21, Fig. 22, Fig. 23.

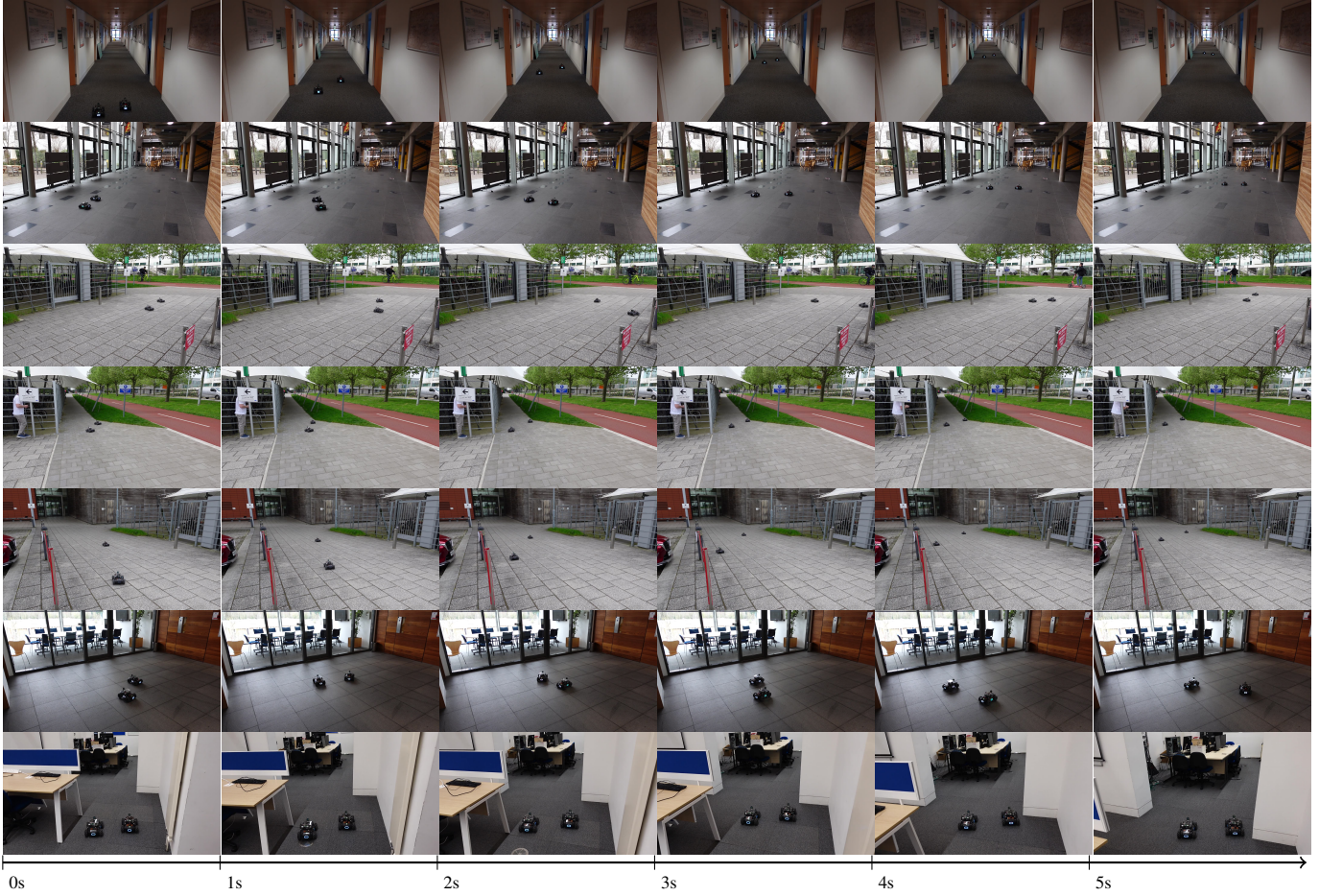


Fig. 11. We show additional snapshots of real-world deployments in different scenes with up to four robots. Each row contains six frames from a video recording, each spaced 1 s in time.

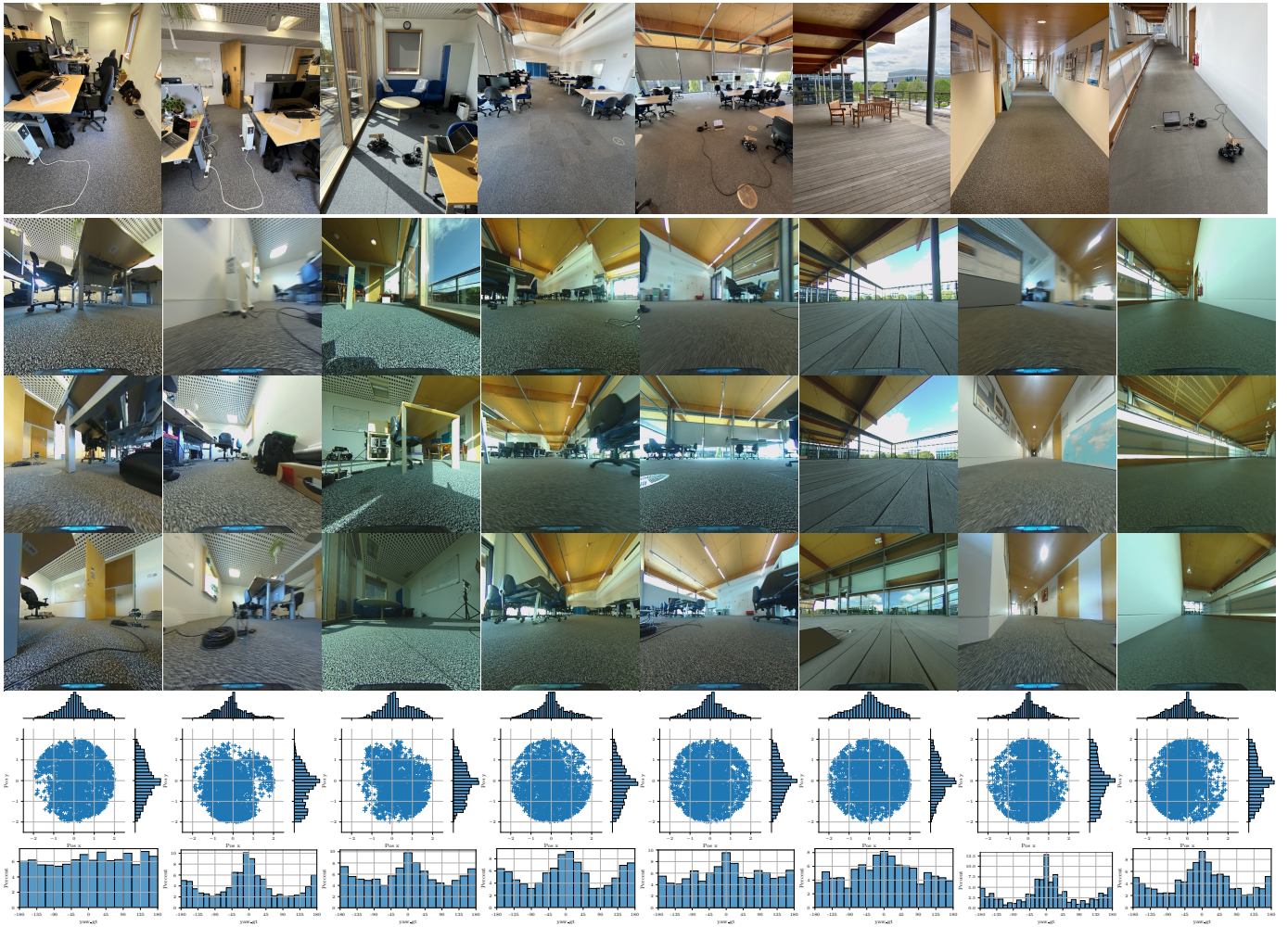


Fig. 12. We collect the real-world dataset $\mathcal{D}_{\text{Test}}^{\text{Real}}$ from five unique scenes in an indoor office building. The scenes show different challenges, from cluttered environments over scenes with high ceilings to sunny floors. We show the distribution of positions for each scene (second row) and the distribution of relative angles between nodes (third row).

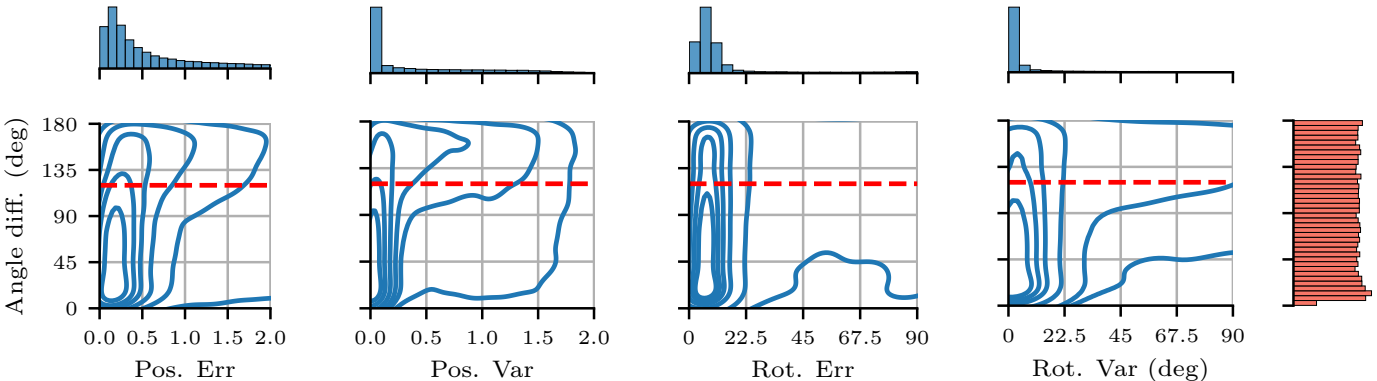


Fig. 13. We show qualitative distributions for position and rotation errors and variances over the relative angle between two robots on all edges of the simulation testset $\mathcal{D}_{\text{Test}}^{\text{Sim}}$. Two agents facing the same direction would have an angle difference of 0° , whereas two agents facing the opposite direction would have an angle difference of 180° . We show the FOV as dashed line, where any results below the line indicate that the edge has some image overlap and above no image overlap. The horizontal marginals show the distribution of each individual plot while the vertical marginal shows the distribution of angle differences over the dataset. While the position error and variance increase over the threshold, the majority of the predictions are still useful. The rotation error is consistent across angle differences, while the uncertainty increases.

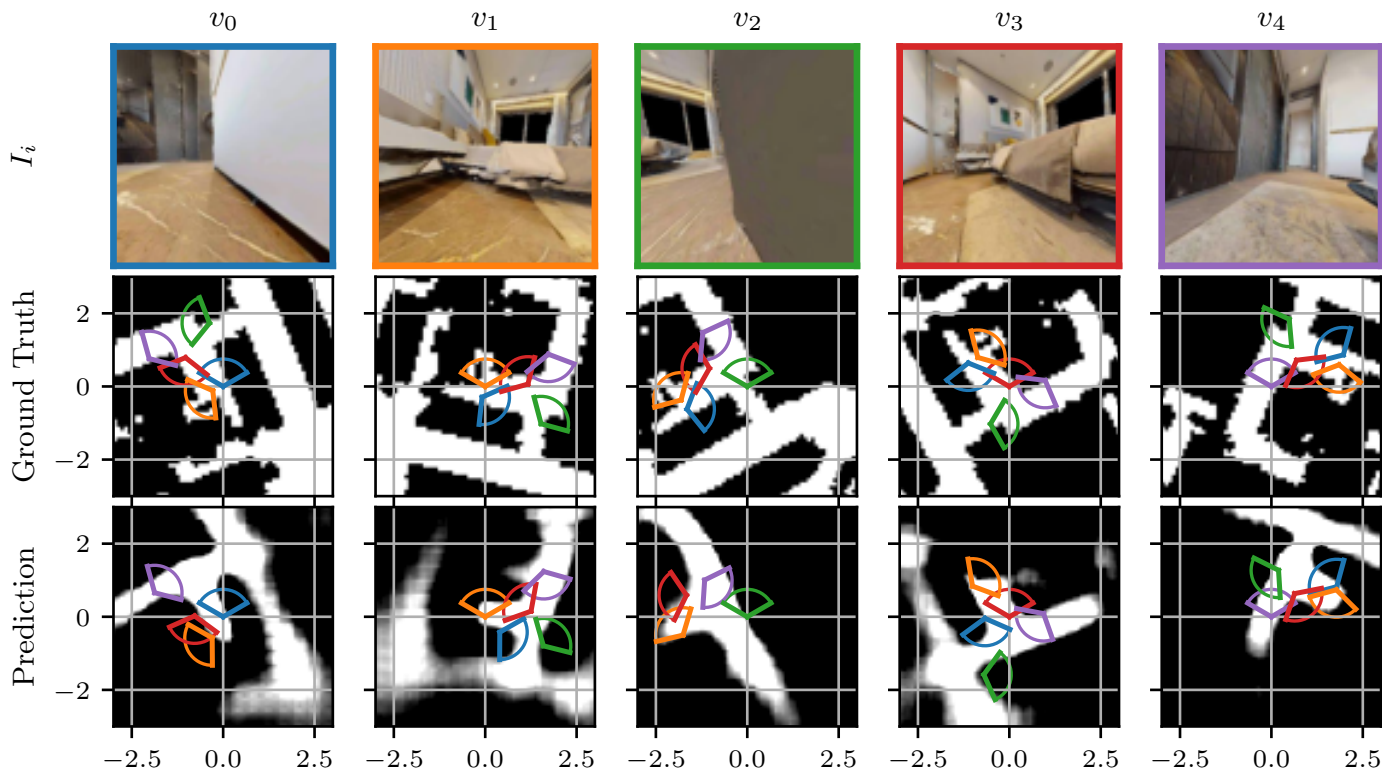


Fig. 14. Sample A from $\mathcal{D}_{\text{Test}}^{\text{Sim}}$.

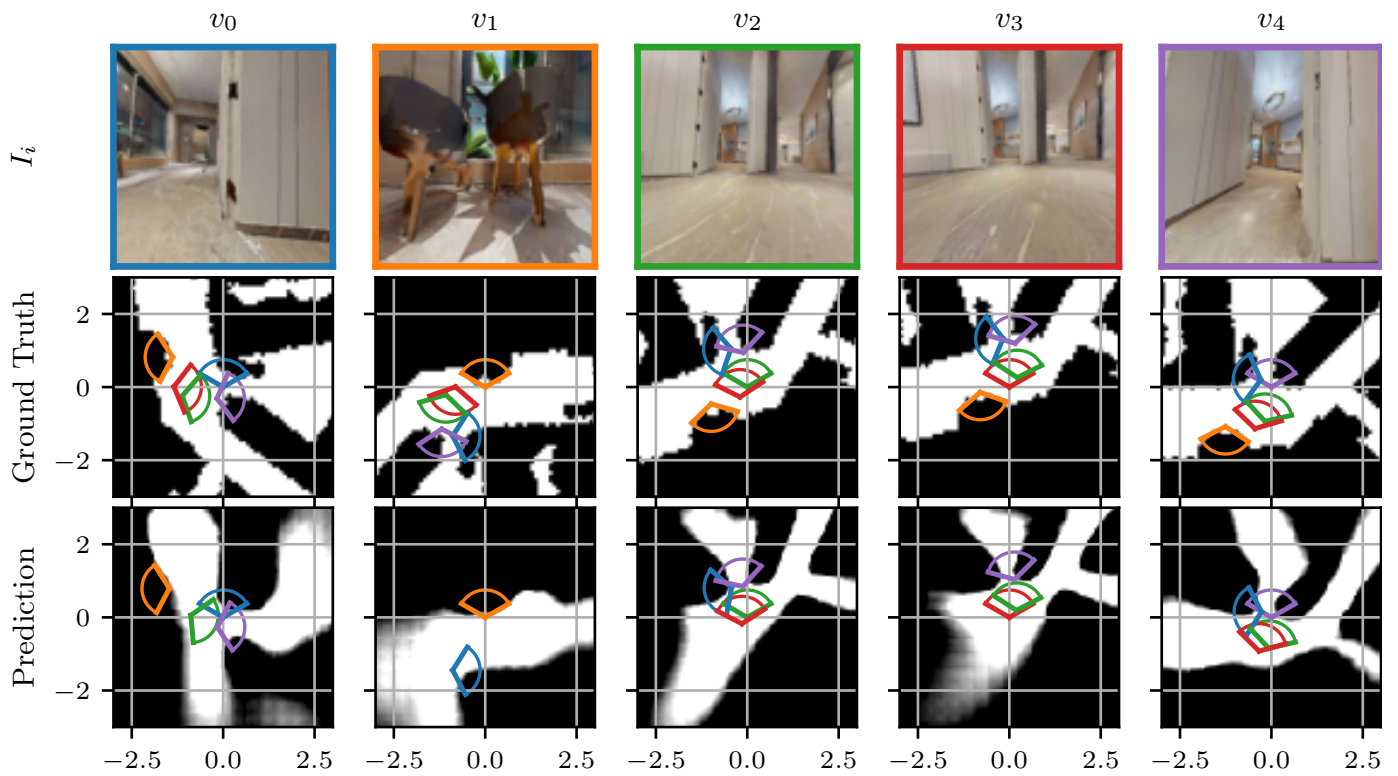


Fig. 15. Sample B from $\mathcal{D}_{\text{Test}}^{\text{Sim}}$.

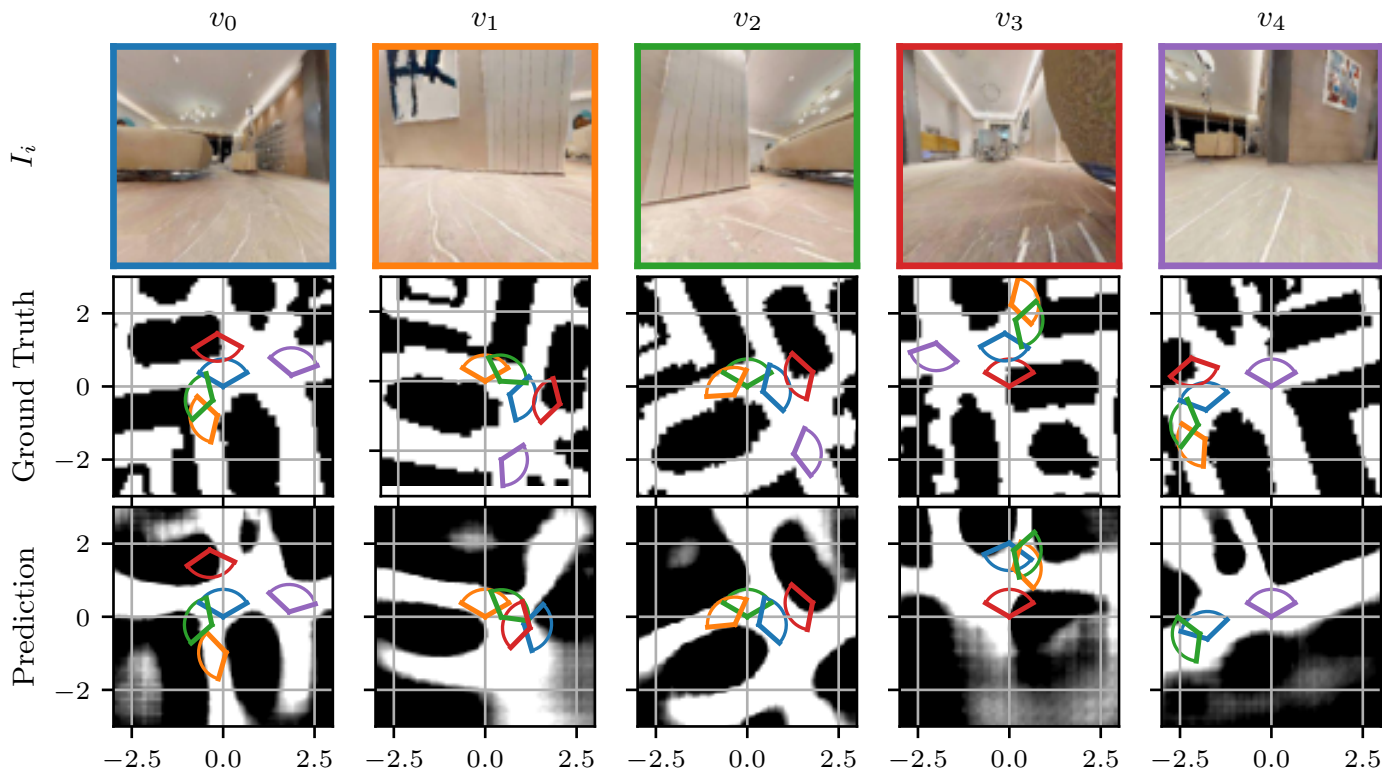


Fig. 16. Sample C from $\mathcal{D}_{\text{Test}}^{\text{Sim}}$.

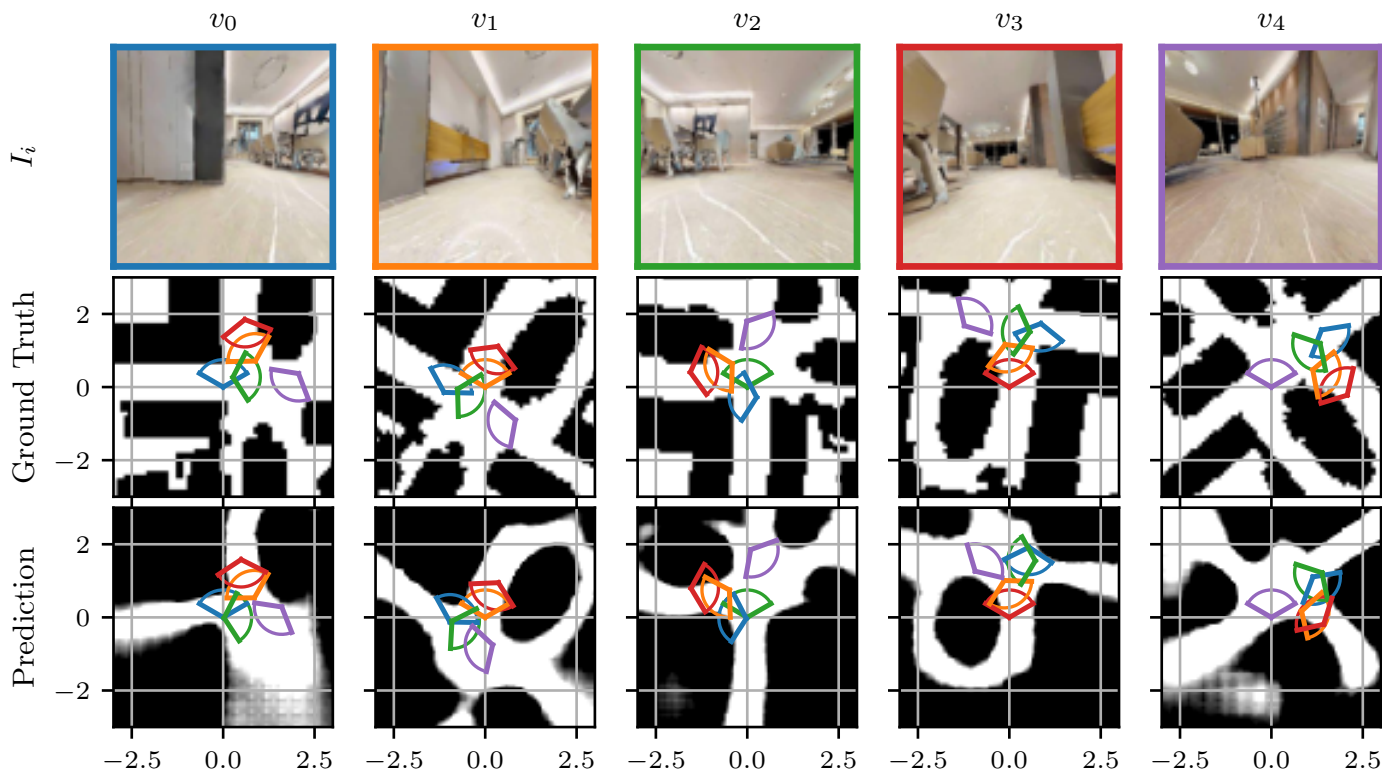


Fig. 17. Sample D from $\mathcal{D}_{\text{Test}}^{\text{Sim}}$.

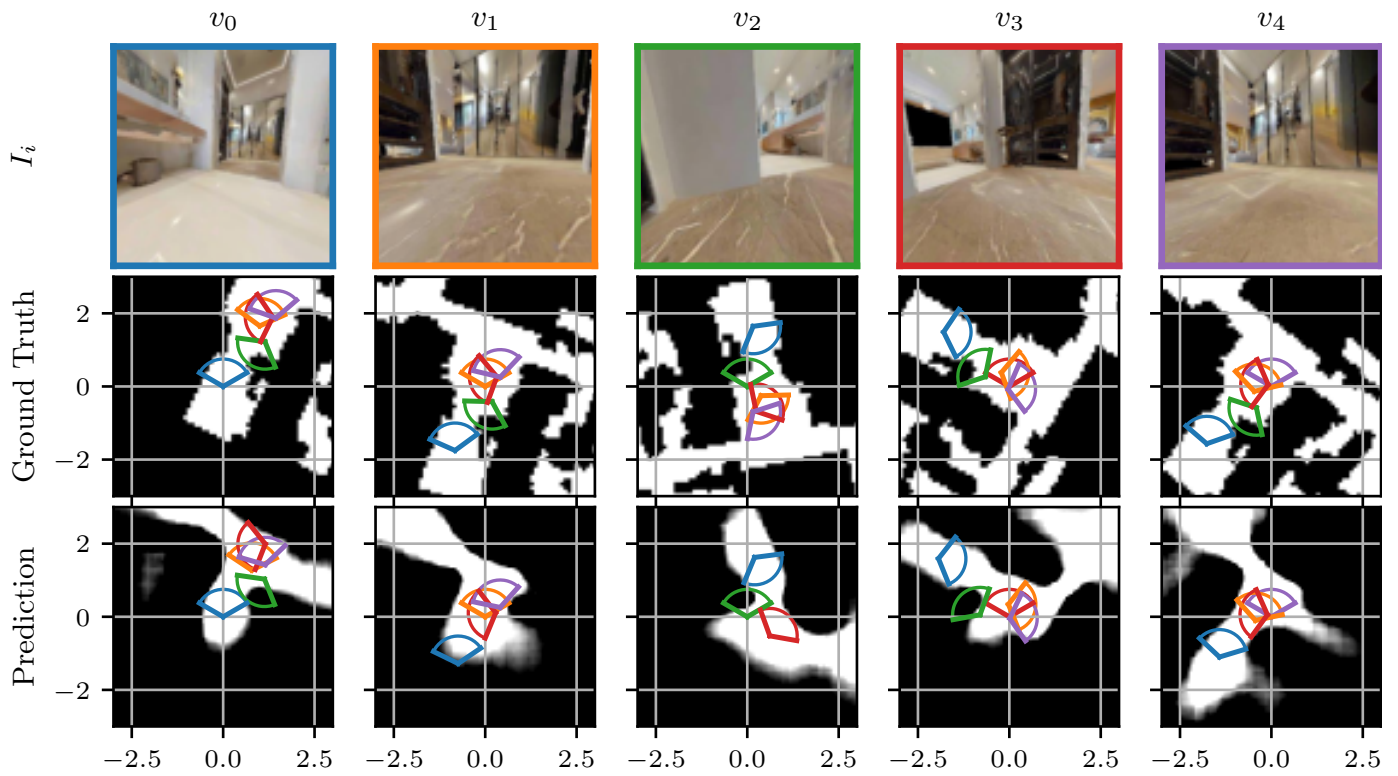


Fig. 18. Sample E from $\mathcal{D}_{\text{Test}}^{\text{Sim}}$.

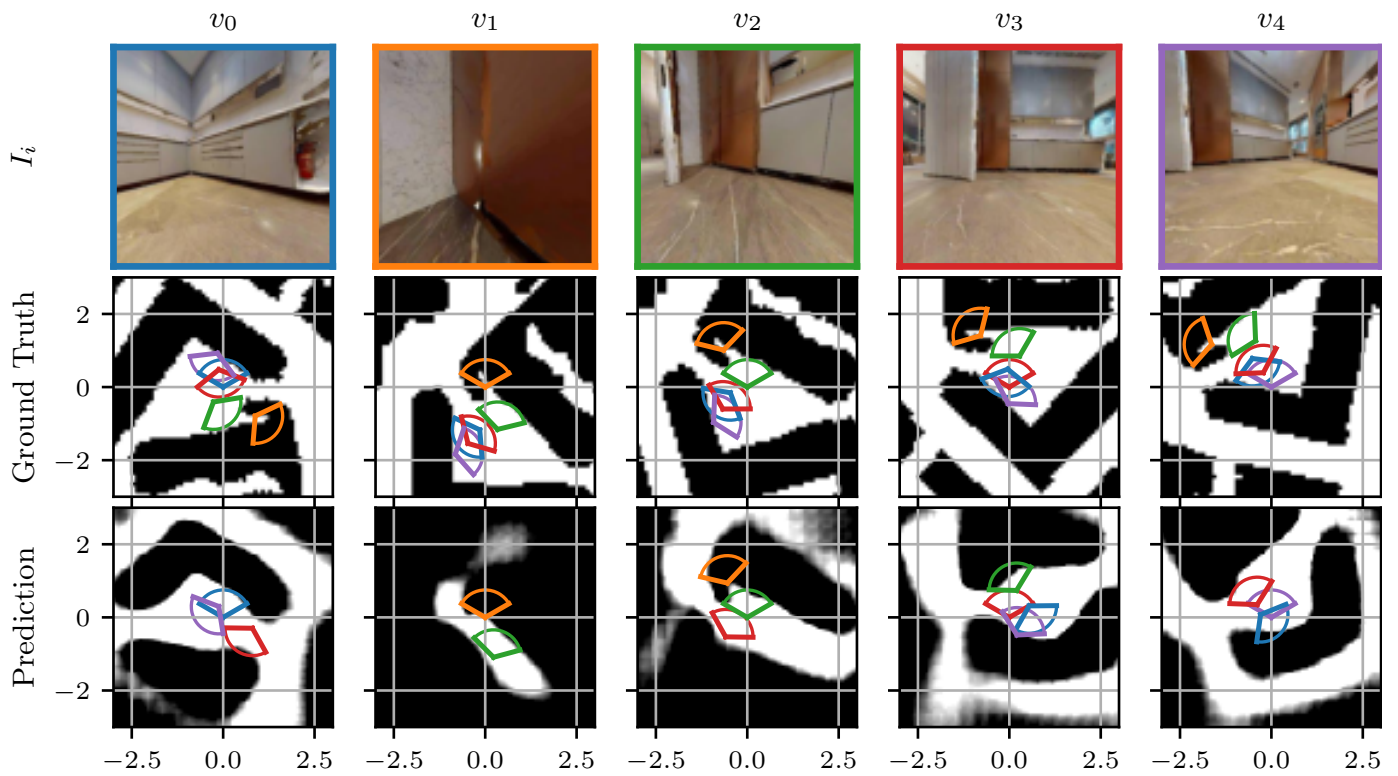


Fig. 19. Sample F from $\mathcal{D}_{\text{Test}}^{\text{Sim}}$.

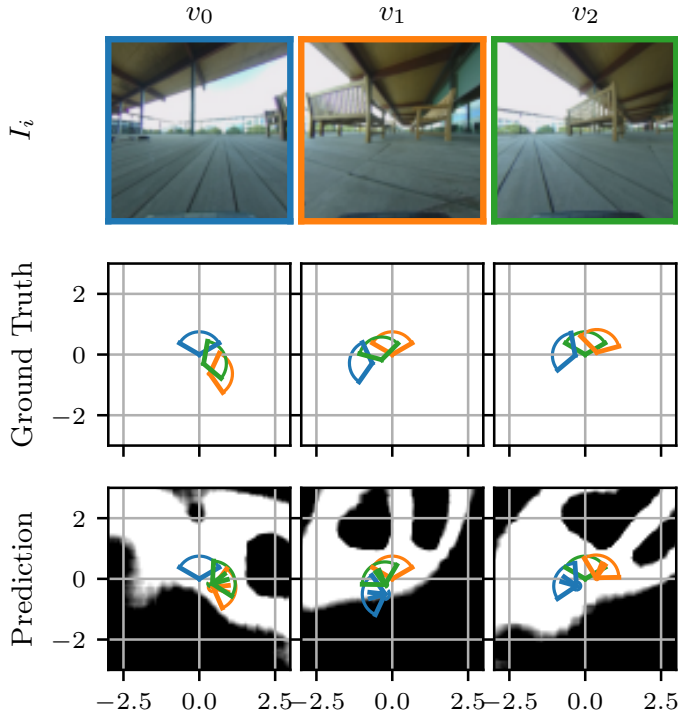


Fig. 20. Sample A from $\mathcal{D}_{\text{Test}}^{\text{Real}}$.

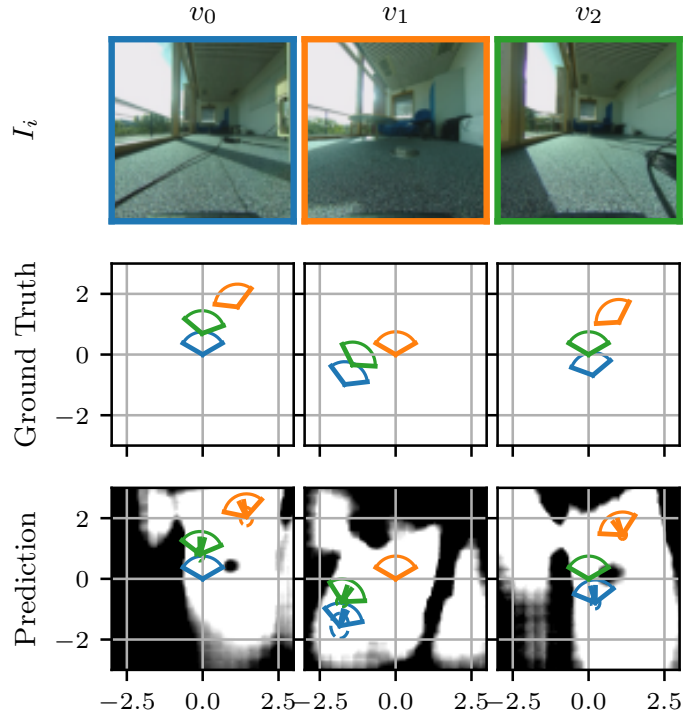


Fig. 22. Sample C from $\mathcal{D}_{\text{Test}}^{\text{Real}}$.

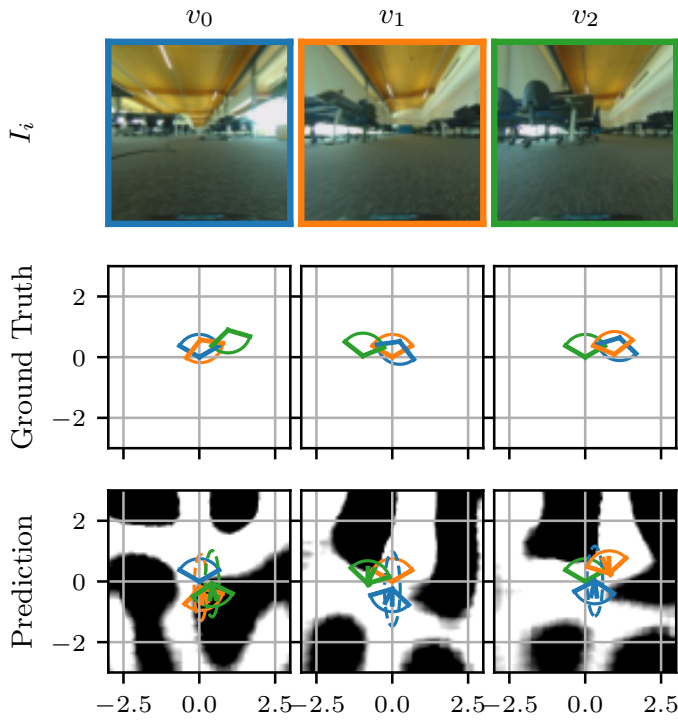


Fig. 21. Sample B from $\mathcal{D}_{\text{Test}}^{\text{Real}}$.

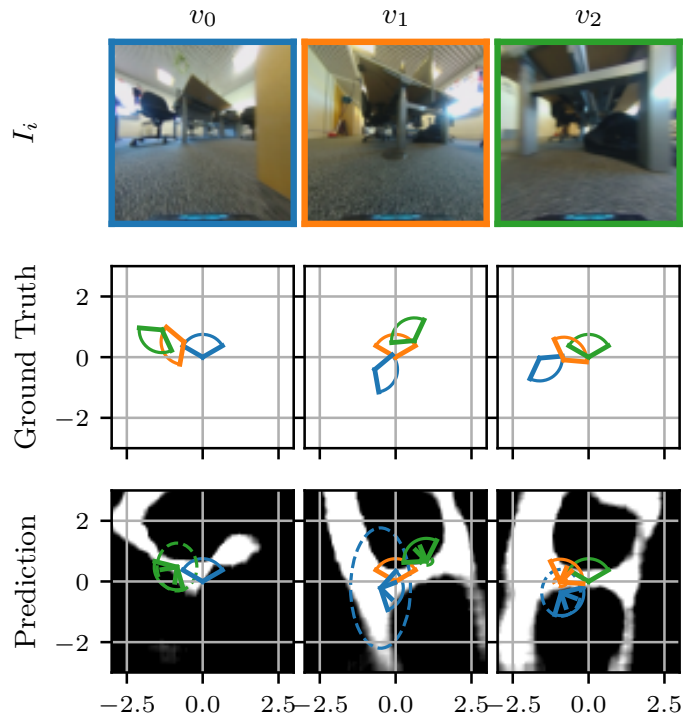


Fig. 23. Sample D from $\mathcal{D}_{\text{Test}}^{\text{Real}}$.